AD_____

Award Number: W81XWH-09-1-0299

TITLE:Photoacoustic Imaging of Epilepsy

PRINCIPAL INVESTIGATOR: Huabei Jiang, PhD

CONTRACTING ORGANIZATION: University of Florida
                          Gainesville, FL 32611

REPORT DATE: April 2012

TYPE OF REPORT: Annual

PREPARED FOR: U.S. Army Medical Research and Materiel Command
               Fort Detrick, Maryland 21702-5012

DISTRIBUTION STATEMENT:

     Á Approved for public release; distribution unlimited

REPORT DOCUMENTATION PAGE

1. REPORT DATE *(DD-MM-YYYY)*	2. REPORT TYPE	3. DATES COVERED *(From - To)*
April 2012	Annual	1 April 2011 - 31 March 2012

4. TITLE AND SUBTITLE	5a. CONTRACT NUMBER
Photoacoustic Imaging of Epilepsy	5b. GRANT NUMBER
	W81XWH-09-1-0299
	5c. PROGRAM ELEMENT NUMBER

6. AUTHOR(S)	5d. PROJECT NUMBER
Huabei Jiang, PhÈDÈ	5e. TASK NUMBER
	5f. WORK UNIT NUMBER

7. PERFORMING ORGANIZATION NAME(S) AND ADDRESS(ES)	8. PERFORMING ORGANIZATION REPORT NUMBER
University of Florida Biomedical Sciences Building Gainesville, FL 32611	

9. SPONSORING / MONITORING AGENCY NAME(S) AND ADDRESS(ES)	10. SPONSOR/MONITOR'S ACRONYM(S)
U.S. Army Medical Research and Materiel Command Fort Detrick, Maryland	
	11. SPONSOR/MONITOR'S REPORT NUMBER(S)

12. DISTRIBUTION / AVAILABILITY STATEMENT

Approved for public release; distribution unlimited

13. SUPPLEMENTARY NOTES

14. ABSTRACT

This research is aimed at developing a new imaging approach, called "Photoacoustic tomography (PAT)", for non-invasively tracking dynamical changes during seizure occurrence. The project will develop imaging hardware and software, and conduct phantom/in vivo experiments to achieve the proposed goals. During the third year of this project, we have developed the advanced boundary conditions scheme, and implemented the 3D reconstruction codes and their parallelization which allowed efficient high performance PAT image reconstruction. We have conducted simulation and phantom experiments that confirmed our software enhancement. We have performed extensive *in vivo* experiments using the rat epilepsy model to evaluate the PAT system we developed in this project. The results show that we were able to image the functional anatomy of epileptic foci noninvasively and in real time at a spatial resolution of ~150μm.

15. SUBJECT TERMS
Photoacoustic imaging, photoacoustic tomography, epilepsy, seizure

16. SECURITY CLASSIFICATION OF:			17. LIMITATION OF ABSTRACT	18. NUMBER OF PAGES	19a. NAME OF RESPONSIBLE PERSON USAMRMC
a. REPORT U	b. ABSTRACT U	c. THIS PAGE U	UU	67	19b. TELEPHONE NUMBER *(include area code)*

Table of Contents

Introduction

Approximately 2.5 million Americans live with epilepsy and epilepsy-related deficits today, more than disabled by Parkinson disease or brain tumors. The impact of epilepsy in the US is significant with a total cost to the nation for seizures and epilepsy of approximately $12.5 billion. Epilepsy consists of more than 40 clinical syndromes affecting 40 million people worldwide. Approximately 25 percent of individuals receiving antiepileptic medication have inadequate seizure control; however, 80% individuals with medication resistant epilepsy might be cured through surgery if one were able to precisely localize the seizure focus. The proposed research will significantly advance our ability to localize such foci, and thereby offer curative epilepsy surgery for this devastating disease. Photoacoustic tomography (PAT) uniquely combines the high contrast advantage of optical imaging and the high resolution advantage of ultrasound imaging in a single modality. In addition to high resolution structural information, the proposed PAT is also able to provide functional information that are strongly correlated with regional or focal seizure activity, including blood volume and blood oxygenation because of the high sensitivity of optical contrast to oxyhemoglobin and deoxyhemoglobin concentrations. The hypothesis of the proposed research is that PAT offers the possibility to non-invasively track dynamical changes during seizure occurrence. The overall goal of this research is to advance a finite element based photoacoustic tomography method for epilepsy imaging, using both laboratory and in vivo experiments. Specifically, in this project we propose**:** (1) To design, construct and test a transducer array system for both 2D and 3D PAT imaging; (2) To advance reconstruction algorithms and associated image enhancement schemes for quantitative PAT; (3) To evaluate and optimize the integrated functioning of the hardware and software components of the transducer array-based system, using simulation and phantom experiments; (4) To test and validate the PAT system using a well established animal model of temporal lobe epilepsy.

Body

This report describes work accomplished in Year 3 (Months 25-36) of the project. As outlined in the approved Statement of Work (SOW), the tasks during this period of time include: **Task 5.** Months 25-42: Implement reconstruction codes in the areas of advanced boundary conditions, 3D algorithms and parallelization of 3D codes; perform simulation and phantom experiments to evaluate the software developments. **Task 6.** Months 25-42: Conduct animal experiments for evaluating the PAT imaging system.

The sections below consist of (1) software development, and (2) animal experiments that reflect the tasks associated with the SOW during Months 25-36.

1. Software Development (Task 5)

We are pleased to report that we have completed the software development proposed for Year 3 including advanced boundary conditions, 3D algorithms, parallelization of 3D codes, and their testing using simulation and phantom experiments.

1.1 Advanced Boundary Conditions

1.1.1 Higher–order absorption boundary conditions

Our PAT reconstruction algorithm uses a regularized Newton iterative strategy to update an initial optical or acoustic properties distribution to minimize an object function composed of a weighted sum of the squared difference between computed and measured acoustic data. The computed acoustic data is obtained by solving the Helmholtz photoacoustic wave equation using finite element method. In the frequency domain, the photoacoustic wave equation (governing equation) can be written,

$$\nabla^2 p(r,\omega) + k_0^2(1+O)p(r,\omega) = ik_0 \frac{c_0 \beta \Phi(r)}{C_p} \tag{1}$$

where p is the pressure wave; $k_0 = \omega/c_0$ is the wave number described by the angular frequency, ω and the speed of acoustic wave in a reference or coupling medium, c_0; O is a coefficient that depends on both acoustic speed and attenuation.

We have implemented the higher-order absorption boundary conditions to improve the model accuracy in Eq. (1). We also compared the reconstructions using higher-order and low-order absorption boundary conditions. For low-order absorption boundary conditions, we apply the Sommerfeld radiation conditions for the Helmholtz wave equation on the boundary,

$$-ik_0 p = \nabla p \cdot \boldsymbol{n} \tag{2}$$

For the higher order case, a second-order absorption boundary conditions for arbitrarily shaped convex artificial boundaries of 3D acoustic problems are also employed here for comparison (Bamberger 1990),

$$-Mp = \nabla p \cdot \boldsymbol{n} \qquad \text{on } \Sigma \tag{3}$$

in which M is differential operator defined as the function of the mean curvature and Gaussian curvature at a point of a surface, Σ is the triangulated surfaces of a 3D linear tetrahedral element.

To test the influence of boundary conditions on the reconstruction accuracy and algorithm performance, 3D simulation tests are conduced here. For the simulation test 1, one 6.0 mm-diameter cylindrical target was embedded in the cylindrical background medium (diameter: 30.0mm; height: 20.0mm), as shown in Fig. 1(a). The absorbed light energy density for the background and target were $\Phi=1$ and $\Phi=3$ (mJ/mm^3), respectively. We can see from Figs. 1(b) and 1(c) that the target was clearly detected by using both the low-order and higher-order absorption boundary conditions. And we found that the impact of the boundary conditions on the recovered absorbed energy density images is not obvious for small target detection.
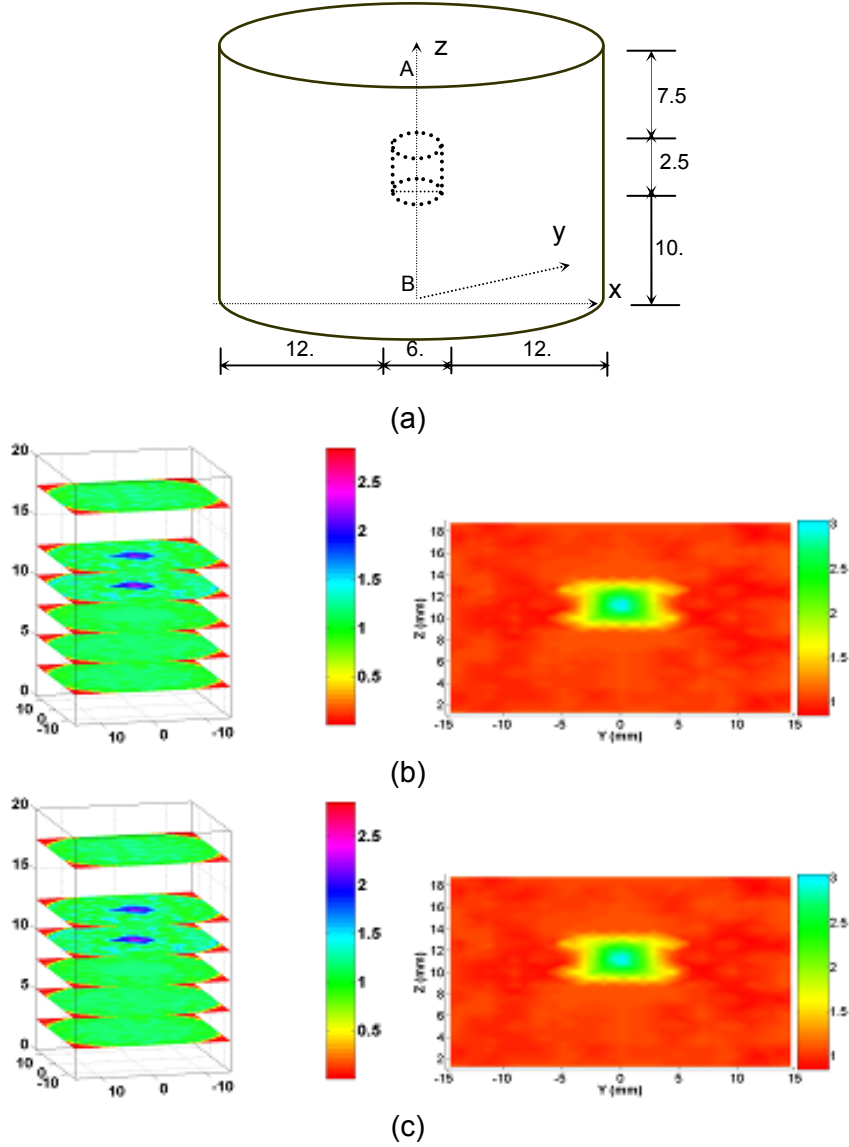
(a)

(b)

(c)

Fig. 1 Reconstructed absorbed energy density images for the one-target case. (a) The Test geometry for the simulation test; (b) both 3D and 2D slice display at x=1.0mm for the recovered energy density with higher-order absorption boundary conditions; (c) both 3D and 2D slice display at x=1.0mm for the recovered energy density with low order absorption boundary conditions. The axes (left and bottom) illustrate the spatial scale, in millimeters, whereas the color scale (right) records the absorbed optical energy density, in mJ/mm^3.

The second test is intended to test the influence of boundary conditions on big target detection. In this case, two 15 mm-diameter cylindrical objects mimicking two seizure focuses were embedded in the background medium where the spacing between the two "focuses" was 2mm. The absorbed light energy density for the background and "seizure focuses" were Φ=1 and Φ=3 (mJ/mm^3), respectively. We can see from Fig. 2 that both the 2 targets can be clearly detected by using both the low-order and high- order absorption boundary conditions. However, the impact of the boundary conditions on the reconstruction of large targets is obvious, where strong boundary artifacts are observed for the reconstruction using the low-order absorption boundary conditions (Fig. 2a).
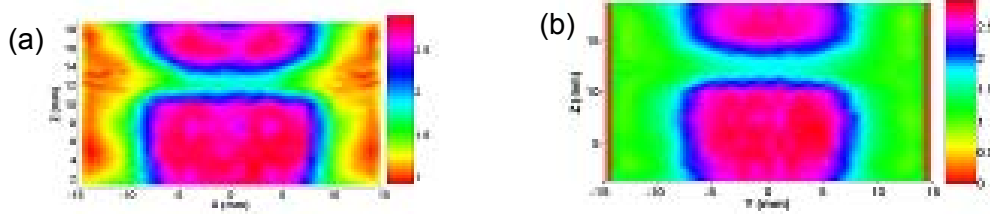
Fig. 2 The recovered absorbed energy density images with the low-order absorption boundary conditions (a), and the higher- order absorption boundary conditions (b).

1.1.2 Mismatches between the computational model and the physical data acquisition

One of our algorithmic development activities will be on issues related to mismatches between the computational model and the physical data acquisition. In this regard we have investigated the possible model representations of the transducers and concomitant boundary conditions. In particular, we implemented a model that considers the finite ultrasound beam effects associated with the receiver hardware. According to the simulation tests, we found that the ultrasound beam size has no effect on the final reconstructed results when our finite element based reconstruction method is used, and the results for a typical test are provided in Fig. 3.
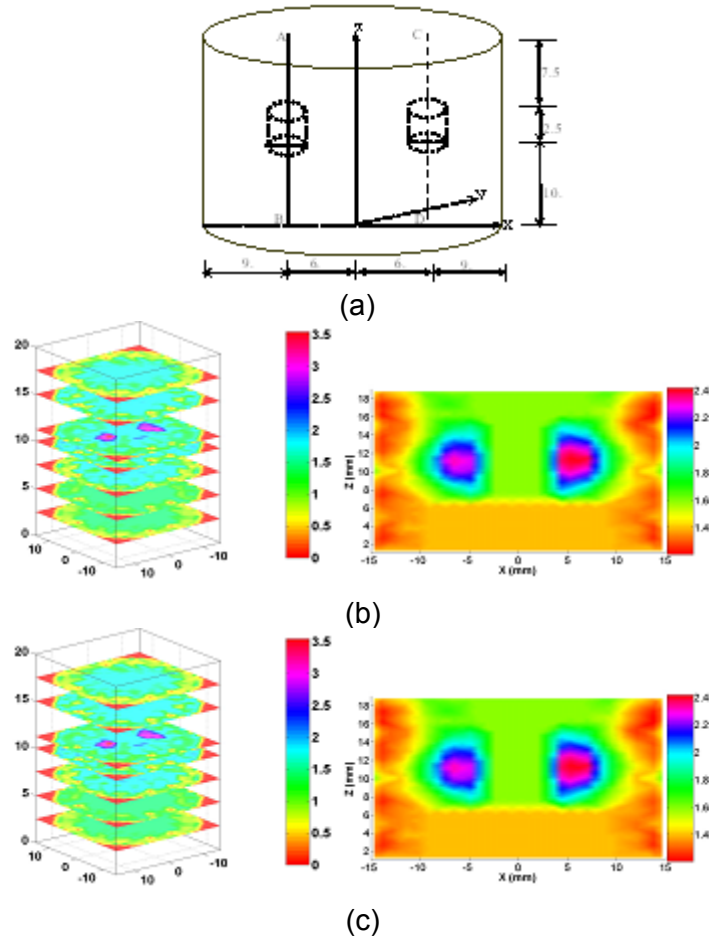
Fig. 3 Reconstructed absorbed energy density images for a two-target case. (a) The test geometry for the simulation test; (b) both 3D and 2D slice display for the recovered energy density using point detectors; (c) both 3D and 2D slice display for the recovered energy density using finite ultrasound beam sizes. The axes (left and bottom) illustrate the spatial scale, in millimeters, whereas the color scale (right) records the absorbed optical energy density, in mJ/mm^3.

4

1.2 3D Algorithms and Parallelization of 3D Codes

1.2.1 3D Algorithms

We have implemented 3D algorithms that can reconstruct the absolute optical absorption coefficient distribution of 3D heterogeneous medium when conventional PAT method is combined with a light transport model. Therefore, the capabilities of PAT have now been extended to provide spatially resolved quantitative physiological and molecular information that can be derived from tissue absorption spectra. Basically, the reconstruction method includes two steps. The first is to obtain the 3D images of absorbed light energy density through our 3D PAT reconstruction algorithm that is based on the finite element solution to the photoacoustic wave equation in frequency domain subject to the radiation or absorbing boundary conditions. The second step is to recover the optical absorption coefficient distribution using the photon diffusion model coupled with the absorbed optical energy density images obtained from the first step.

In the first step, our 3D PA reconstruction algorithm uses a regularized Newton iterative strategy to update an initial absorbed optical energy density distribution to minimize an object function composed of a weighted sum of the squared difference between computed and measured acoustic data. In the second step, to recover the optical absorption coefficient from the absorbed energy density, Φ, the photon diffusion equation as well as the Robin boundary conditions can be written in consideration of $\Phi = \mu_a \Psi$,

$$\nabla \cdot D(r)\nabla\big(E(r)\Phi(r)\big) - \Phi(r) = -S(r) \tag{4}$$

$$-D\nabla\big(E(r)\Phi\big)\cdot n = E(r)\alpha\Phi \tag{5}$$

where $E(r) = 1/\mu_a(r)$, $D(r)$ is the diffusion coefficient and $D = 1/(3(\mu_a + \mu_s'))$ where μ_s' is the reduced scattering coefficients, α is a boundary condition coefficient related to the internal reflection at the boundary, and $S(r)$ is the incident point or distributed source term. For the inverse computation, the so-called Tikhonov-regularization sets up a weighted term as well as a penalty term in order to minimize the squared differences between computed and measured absorbed energy density values,

$$\min_{\chi}\left\{\left\|\mathbf{\Phi}^c - \mathbf{\Phi}^o\right\|^2 + \beta\left\|\mathbf{L}[\mathbf{E} - \mathbf{E}_0]\right\|^2\right\} \tag{6}$$

where $\mathbf{L}$ is the regularization matrix or filter matrix, β is the regularization parameter, $\mathbf{\Phi}^o = (\Phi_1^o, \Phi_2^o, ..., \Phi_N^o)^{\mathrm{T}}$ and $\mathbf{\Phi}^c = (\Phi_1^c, \Phi_2^c, ..., \Phi_N^c)^{\mathrm{T}}$ where Φ_i^o is the absorbed energy density obtained from PAT, and Φ_i^c is the absorbed energy density computed from Eqs. (4) and (5) for i=1, 2..., N locations within the entire PAT reconstruction domain. The initial estimate of absorption coefficient can be updated based on iterative Newton method as follows with β=1,

$$\Delta(\mathbf{E}) = (\mathbf{J}^T\mathbf{J} + \lambda\mathbf{I} + \mathbf{L}^T\mathbf{L})^{-1}[\mathbf{J}^T(\mathbf{\Phi}^o - \mathbf{\Phi}^c)] \tag{7}$$

in which Laplacian-type filter matrix, $\mathbf{L}$, is employed and its elements are written,

$$L_{ij} = \begin{cases} 1 & if \quad i = j \\ -1/NN & if \quad i, j \subset one \quad region \\ 0 & if \quad i, j \subset diffrent \quad region \end{cases} \qquad (8)$$

where *NN* is the total node number within one region or tissue. The optical absorption coefficient distribution is then reconstructed through the iterative procedures described by Eqs. (4) and (7) where *a priori* spatial information from the PAT image is incorporated in through the matrix **L**.

Phantom experiments were conducted to test the 3D algorithms using the 192-channel PAT system developed in Years 1 and 2. The 3D phantom was made of Intralipid, India ink, distilled water and Agar powder. For the phantom, the two "seizure focuses" had: (absorption coefficient) μ_a = 0.07mm^{-1}, (reduced scattering coefficient) μ_s' =2.5mm^{-1} and a diameter of 6mm, and the soft tissues between the seizure focuses had: μ_a = 0.015mm^{-1}, and μ_s' =1.5mm^{-1}.

The reconstructed results for the phantom experiment are shown in Fig. 4, where Fig. 4a displays the coronal cross section of the reconstructed 3D absorbed energy density image. We can observe that the seizure focuses are clearly identified (the red area). The recovered absorption coefficient image is displayed in Fig 4b, where the targets are recovered in terms of the position, size and quantitative optical property.
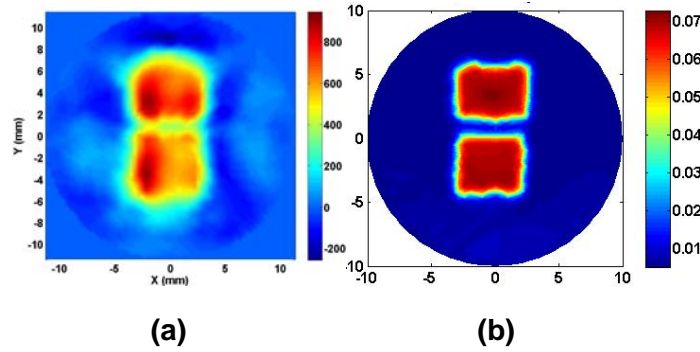

(a)　　　　　　　**(b)**

Fig. 4 (a) The selected coronal slice from the recovered absorbed energy density image, (b) the selected coronal slice from the recovered absorption coefficient image.

1.2.2 Parallelization of 3D reconstruction codes

As we have experienced, full 3D reconstruction requires significant computational times especially at higher ultrasound frequencies. Given the large problem size, three major areas of the algorithm are costly: *(i)* computation of the forward solution, *(ii)* buildup of the Jacobian matrix which requires calculation of the derivatives of acoustic field with respect to optical/acoustic properties at the receiver sites, and *(iii)* computation of a full matrix equation for the inverse solution. Because of the massively parallel structure of these types of image reconstruction algorithms, parallel computing was adapted for our 3D PAT reconstruction and the code was developed to resolve this large-scale computational problem.

Parallel computing is basically the concurrent execution of many computations using many processors. In a parallel computing scheme, the memory request and the computation tasks for a computation assignment can be spread on multiple processors as shown in Fig. 5. In the following, we will give a detailed description on the parallel computing based 3D PAT algorithm.

In the finite element based PAT algorithm, the forward calculation of acoustic field and the determination of Jacobian matrix J are based on the forward matrix A at each frequency ω_i, ordered from ω_1 to ω_K with total K frequency elements. The matrix A in forward equations is usually a symmetric sparse matrix and stored in memory by banded storage or compressed storage strategy, requiring less memory than the Jacobian matrix J and the Hessian matrix $J^\mathrm{T}J$, which is usually a full matrix. Herein, we spread the forward calculation of acoustic field and the determination of Jacobian matrix on distributed processors (total number is $Q+1$) by the frequency element ω_i, where the whole matrix A under certain frequency elements is stored in the memory of the specifically assigned processor. As shown in flow chart of the high performance photoacoustic tomography (Fig. 6), the matrix A at frequency ω_i is stored in the memory of a processor determined by $Mod(i-1,L)$, where L is the average number of frequency elements on each processor (total frequency elements K divided by total processors $Q+1$). In each processor, the forward modeled acoustic field as well as the elements of Jacobian matrix at the frequencies associated with the specified processor is calculated independently, after which the Jacobian matrix J over the whole frequency range is assembled and stored dispersedly in the memories of the distributed processors. In this way of parallel computing and storage, the computation load and storage is evenly assigned among the processors, and the computation assignment is maximally parallelized since each processor can run the assigned task independently without communication with other processors.

Jacobian matrix J and the Hessian matrix $J^\mathrm{T}J$ (denoted as H) are full matrices, requiring distributed storage over the processors. A wrapping storage over the columns of the Jacobian matrix J is used to evenly store the Jacobian sub-matrix over the processors and further efficiently calculate the Hessian matrix H with minimally mutual communication between the processors. The wrapping storage is described below,

$$\left\{\vec{J}_j\right\} \in CPU \ Myid, \ if \ Myid = Mod(j-1, Q+1) \tag{9}$$

where $\left\{\vec{J}_j\right\} = \left\{J_{1j},\ldots,J_{Mj},J_{(M+1)j},\ldots,J_{(M\times K)j}\right\}^T$, $j=1,\ldots,N$.

With the wrapping storage of the Jacobian matrix J, the Hessian matrix H can be calculated and stored by

$$\left\{\vec{H}_j\right\} = \left\{\vec{J}_1 \ \vec{J}_2 \cdots \vec{J}_j\right\}^T \left\{\vec{J}_j\right\} \in CPU \ Myid, \ if \ Myid = Mod(j-1, Q+1) \tag{10}$$

where $\left\{\vec{H}_j\right\} = \left\{H_{1j},\ldots,H_{jj}\right\}^T$, $j=1,\ldots,N$.

Because the Hessian matrix H is symmetric, we store only the upper triangle of the Hessian matrix spread over the processors. In the calculation of element H_{ij}, communication and data exchange may be involved among the distributed processors, except that the vector $\left\{\vec{J}_j\right\}$ and $\left\{\vec{J}_j\right\}$ are both stored in the memory of the same processor. Since the Hessian matrix is stored dispersedly, the inverse reconstruction requires a parallel solving method, where parallelized Cholesky decomposition is used in our high performance PAT.

With the high performance PAT, simulated 3D blood vessels with different diameters (0.6mm, 0.28mm and 0.14 mm) can be accurately reconstructed, as shown in Fig. 7 for one slice of the 3D image.
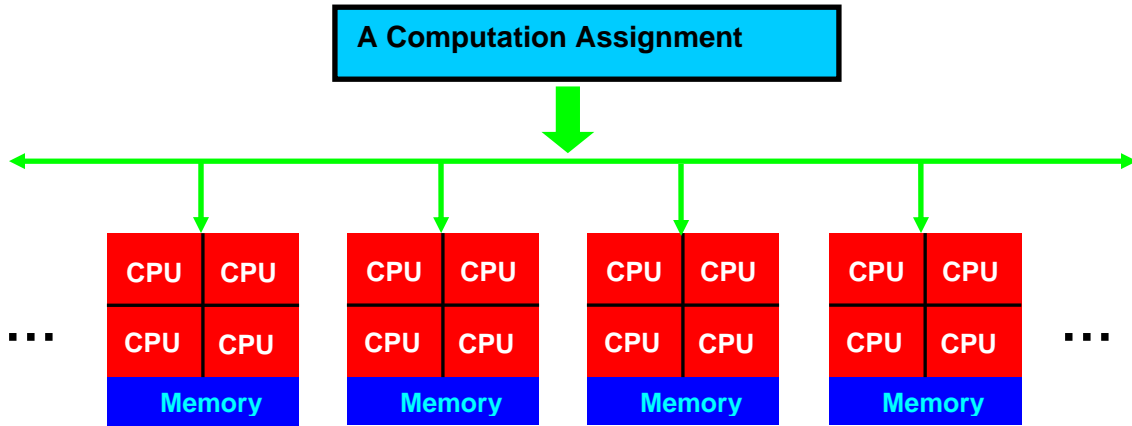

Fig.5 Schematic of parallel computing with a combination of both shared memory and distributed memory.
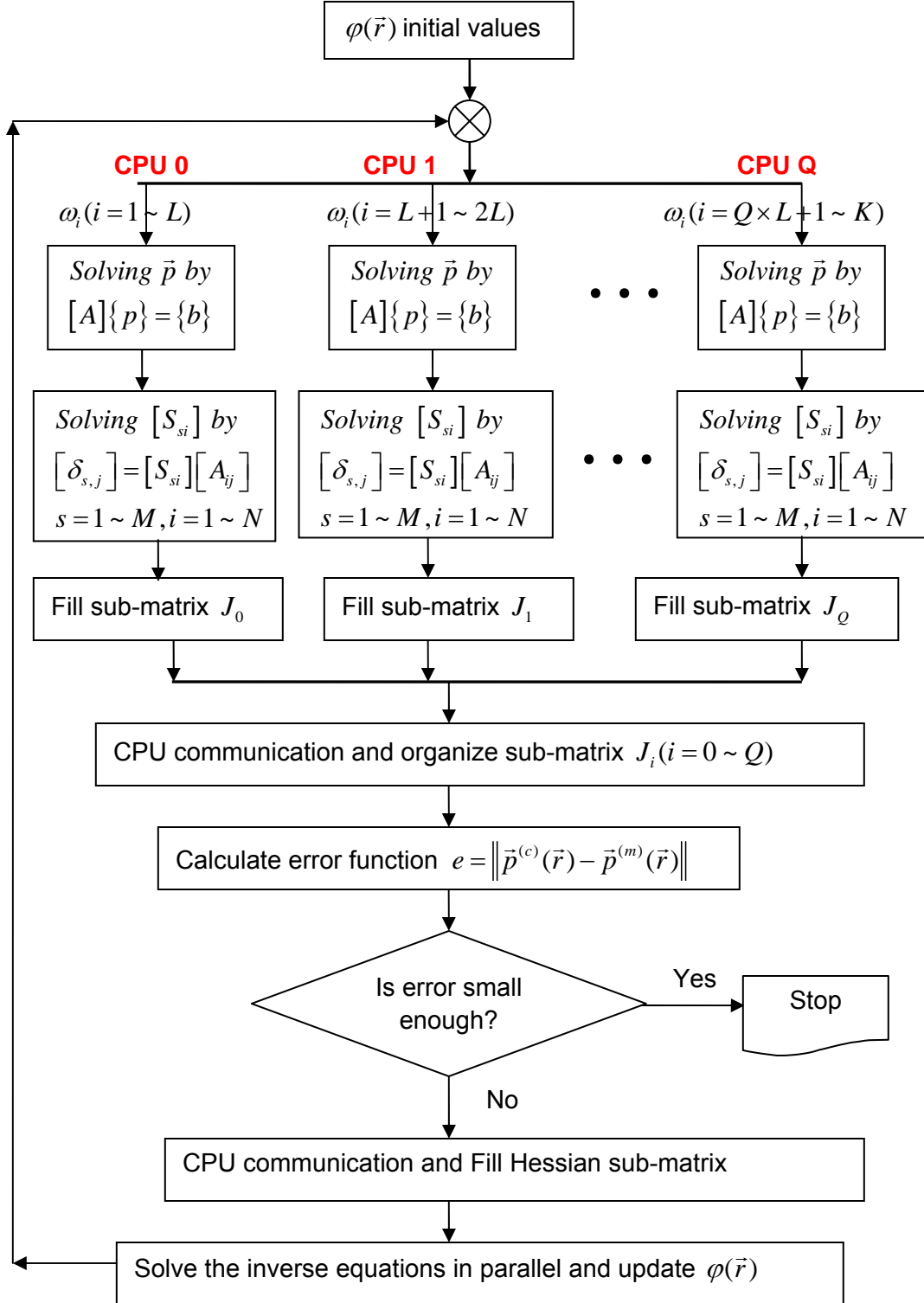
$\varphi(\vec{r})$ initial values

CPU 0 $\omega_i(i=1 \sim L)$

CPU 1 $\omega_i(i=L+1 \sim 2L)$

CPU Q $\omega_i(i=Q \times L+1 \sim K)$

Solving $\vec{p}$ by $[A]\{p\}=\{b\}$

Solving $\vec{p}$ by $[A]\{p\}=\{b\}$

· · ·

Solving $\vec{p}$ by $[A]\{p\}=\{b\}$

Solving $[S_{si}]$ by $[\delta_{s,j}]=[S_{si}][A_{ij}]$ $s=1 \sim M, i=1 \sim N$

Solving $[S_{si}]$ by $[\delta_{s,j}]=[S_{si}][A_{ij}]$ $s=1 \sim M, i=1 \sim N$

· · ·

Solving $[S_{si}]$ by $[\delta_{s,j}]=[S_{si}][A_{ij}]$ $s=1 \sim M, i=1 \sim N$

Fill sub-matrix J_0

Fill sub-matrix J_1

Fill sub-matrix J_Q

CPU communication and organize sub-matrix $J_i(i=0 \sim Q)$

Calculate error function $e=\left\| \vec{p}^{(c)}(\vec{r}) - \vec{p}^{(m)}(\vec{r}) \right\|$

Is error small enough?

Yes → Stop

No

CPU communication and Fill Hessian sub-matrix

Solve the inverse equations in parallel and update $\varphi(\vec{r})$

Fig. 6 Flow chart of the high performance PAT based on parallel computing technique and finite element method.
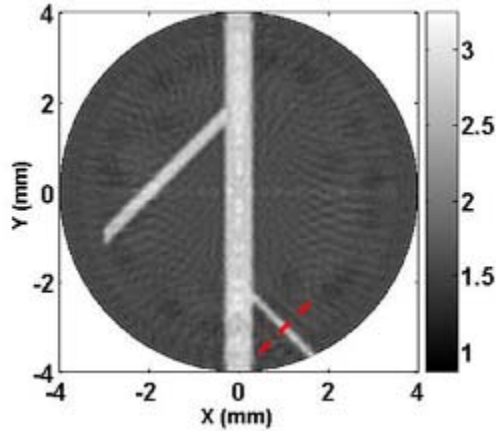
Fig. 7 The reconstructed coronal slice selected from simulated 3D blood vessels.

2. Animal Experiments (Task 6)

In Year 3 we conducted extensive animal experiments to evaluate the PAT system constructed in Years 1 and 2. **We were able to image the functional anatomy of a focal seizure noninvasively and in real time at a spatial resolution of ~150µm (Figs. 8-11).** In this real time PAT system (**Fig. 8a**), light from a Ti: Sapphire laser tunable from 690 to 950 nm was delivered to the cortical brain surface through an optical fiber. Part of the energy of each laser pulse was detected by a photodiode for calibration. A 192-element full-ring transducer array was used to capture the photoacoustic signals generated by the laser light. All the 192 channels were equipped with preamplifiers and secondary stage amplifiers for optimized signal-to-noise ratio. A 3:1 electronic multiplexer coupled with 64-channel analog-to-digital converters completed the 192-channel data acquisition, providing an imaging speed of 0.33 s/frame primarily limited by the 10 Hz laser repetition. The spatial resolution of PAT is inversely related to the bandwidth of the ultrasonic transducer. In our PAT system each ultrasonic detector had a 5 MHz central frequency, a 70% nominal bandwidth, and a diameter of 6 mm (Blatek, Inc., PA, USA), resulting in a spatial resolution of 150µm.

We first tested the PAT system accuracy by imaging a living rat brain with both the scalp and skull intact. Results indicate that the noninvasive PAT image of the rat cortical vasculature correlated with the anatomical location of each vessel (**Figs. 8b, c**). The middle cerebral artery, right hemispheres, left hemispheres, left olfactory bulbs, and right olfactory bulbs were clearly visualized in the PAT image. Numbers 1-5 marked in the image indicate that the micro-blood vessels have diameters of less than 100 µm.

We then tested the system accuracy in identifying a focal EEG seizure and focal EEG epileptogenic spike and wave discharges. Adult Sprague Dawley rats were experimentally prepared to demonstrate focal cortical seizures. 10 µl of 1.9 mM of the GABA antagonist bicuculline methiodide and 10 µl of saline control were injected into the left and right parietal neocortex, respectively. The region of interest including the injection site and remaining skull surface was photoacoustically scanned continuously at time beginning immediately before the electrographic seizure onset time, during the seizure time, and after the seizure ended (**Fig. 9c**). Whereas a significant increase of absorption is seen in the region of the bicuculline injection, no

absorption contrast is observed in the region of the saline injection or surrounding brain areas (**Fig. 9c**). These results suggest that the increase in local and surrounding brain tissue absorption was mostly due to the local bicuculline induced seizures (**Figs. 9d, e**). These results demonstrate the local network of the seizure foci, revealing complex interactions among different neuronal groups at a spatial scale of ~ 100 μm. In summary, these results highlight the accuracy of PAT for noninvasive precise localization of epileptic foci and network.

We also employed PAT to see if we could identify interictal spike and wave epileptiform discharges. Interictal discharges are often seen in focal epilepsy and represent highly synchronized events. Spikes often correlate with the spatial context of an epileptic focus. We recorded PAT imaging from a region of ~2 × 3 mm in the purple area (Marked ROI in **Fig. 10a**). We observed a clear optical absorption change directly associated with de-oxygenation at a wavelength of 755 nm (**Fig. 10c**). At seizure onset at 1min 6.267 s, the focus measured 0.2053 mm^2 and increased to 0.5004 mm^2 during the categorical electrographic seizure spike and wave frequency and amplitude increases (**Fig. 10b**). Corresponding rate changes (0.33 s) spike and wave discharges and PAT images were observed in each experimental trial.

To understand the dynamic interactions within the seizure functional circuitry, we use the frequency domain pairwise Granger analysis to analyze the PAT time series data. The time series data was selected from 200 sets of PAT images sampled at 3Hz within the seizure onset period, and at each time point, we chose nine ROIs (**Fig. 11c$_1$**) and used the averaged optical absorption within each region for the network analysis. The nine sets of time series analysis were classified into 3 groups: (1) the primary ictal onset area and corresponding 4 surrounding regions of interest (ROI); (2) the primary seizure focus, secondary homotopic foci and 2 ROIs surrounding the primary focus in the contralateral cortex; and (3) the middle cerebral artery, primary seizure focus, and secondary homotopic seizure focus. From group 1 analysis, we can see the causal influence from the primary focus to its surrounding ROIs (**Fig. 11b, left**). We also computed the zero-lag correlation between the primary focus and its 4 surrounding ROIs. We found that between the primary focus and ROI 2, there was an obvious negative correlation (-0.68), indicating that the neural activities within these two regions changed in opposite direction over time. Such inverted change in optical signal was likely due to the opposite oxygen delivery or blood flow. **Figure 11c$_2$** shows the Granger analysis for group 2 data where we see that the primary and mirror foci influenced mutually with a stronger influence of primary focus to the mirror focus. Moreover, we observed that the primary focus could also influence the other 2 ROIs in the contralateral hemisphere. Finally, from group 3 analyses (**Fig. 11c$_3$**), we can see that the primary focus strongly influenced the hemodynamic change in the middle cerebral artery, which in turn showed influence on the secondary homotopic foci.
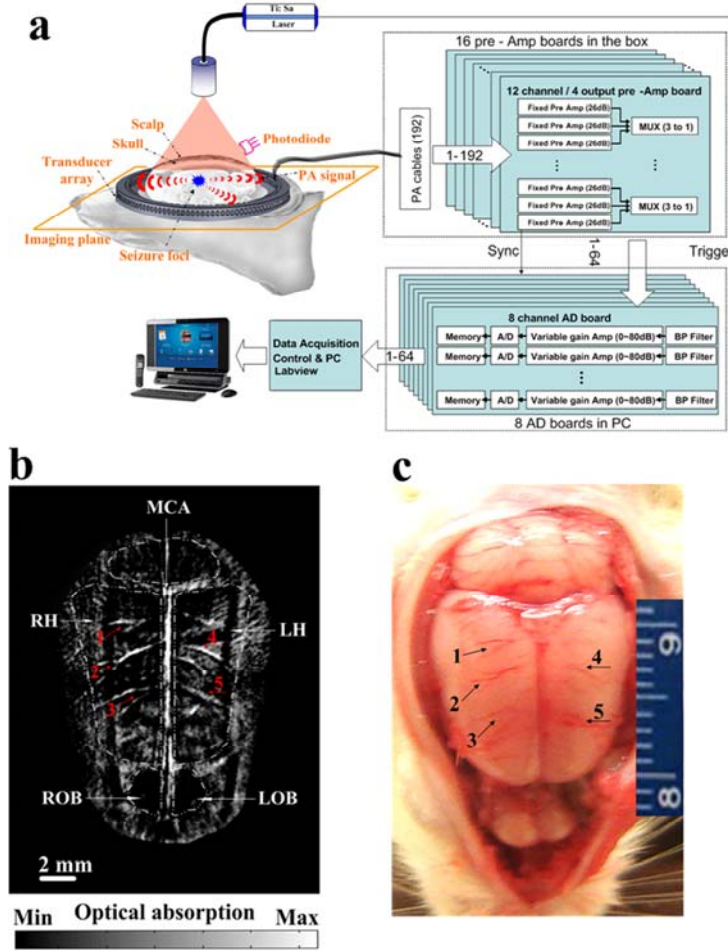
Figure 8 Real-time PAT system for seizure dynamics. (a) Schematic of the real-time PAT system. A 192-element full-ring transducer array was used to capture the PA signal during seizure onset. **(b)** Noninvasive PAT imaging of a rat brain *in vivo* <u>with the skin and skull intact</u>. MCA, middle cerebral artery; RH, right hemispheres; LH, left hemispheres; LOB, left olfactory bulbs; ROB, Right olfactory bulbs. **(c)** Open-skull photograph of the rat brain surface acquired <u>after</u> the PAT experiment. Numbers 1–5 indicate the corresponding blood vessels in the PAT image and rat brain photograph.
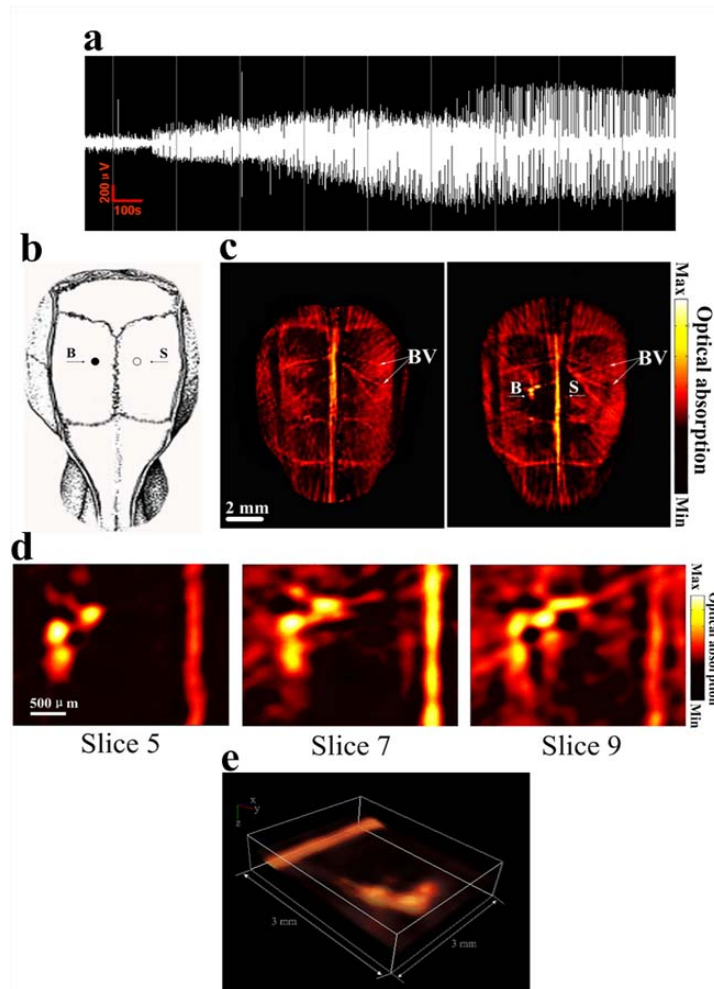
Figure 9 Noninvasive epileptic foci localization. (a) EEG recordings of seizure onset after bicuculline methiodide injection. **(b)** Schematic showing the location of BMI injection and saline injection (control). B, BMI injection; S, saline injection. **(c)** Reconstructed PAT image before (left) and after (right) the bicuculline methiodide injection. The BMI and saline were injected into the left and right parietal neocortex, respectively. A significant increase of optical absorption is seen in the region of the bicuculline methiodide injection, while no absorption contrast is observed in the region of the saline injection relative to its surroundings. **(d)** Series of PAT images from three representative transverse planes parallel to the skin surface with 755 nm wavelength. Slices 5, 7, and 9 are the images obtained 3, 5 and 7 mm under the skin, respectively. The images show different spatial patterns at the seizure foci at different tomographic layers. **(e)** Three dimensional rendering of the epileptic foci from different tomographic layers.
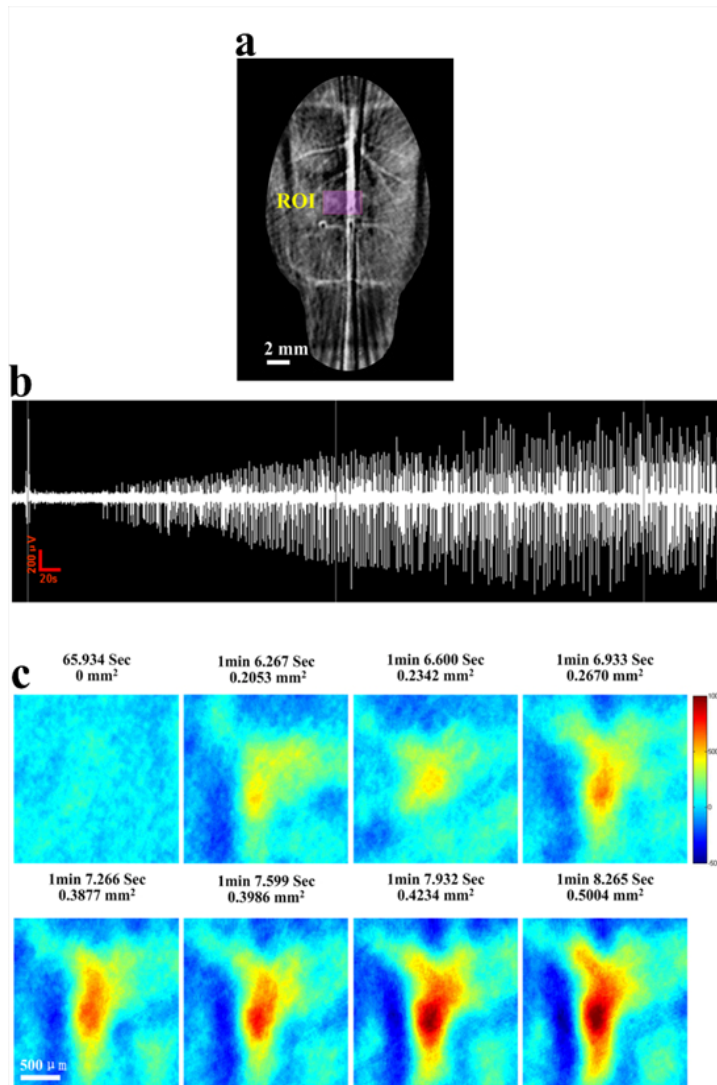
Figure 10 Real-time monitoring of ictal onset. (a) A PAT image showing the cerebral vasculature and the position of BMI injection. ROI, region of interest; Scale bar: 2mm. **(b)** EEG recordings showing the seizure onset about 1 min after BMI injection. **(c)** PAT images recording the ictal onset in real time. At 1min 6.267 s the area of the focus was 0.2053 mm^2. The area of the focus then increased in size over the next 2 s to 0.5004mm^2, corresponding to an increase in the amplitude of the EEG spikes. The area of the seizure focus was derived from the PAT images by thresholding to a pixel value one standard deviation above the pixel values from the area of the focus during the control conditions. Scale bar: 500µm.
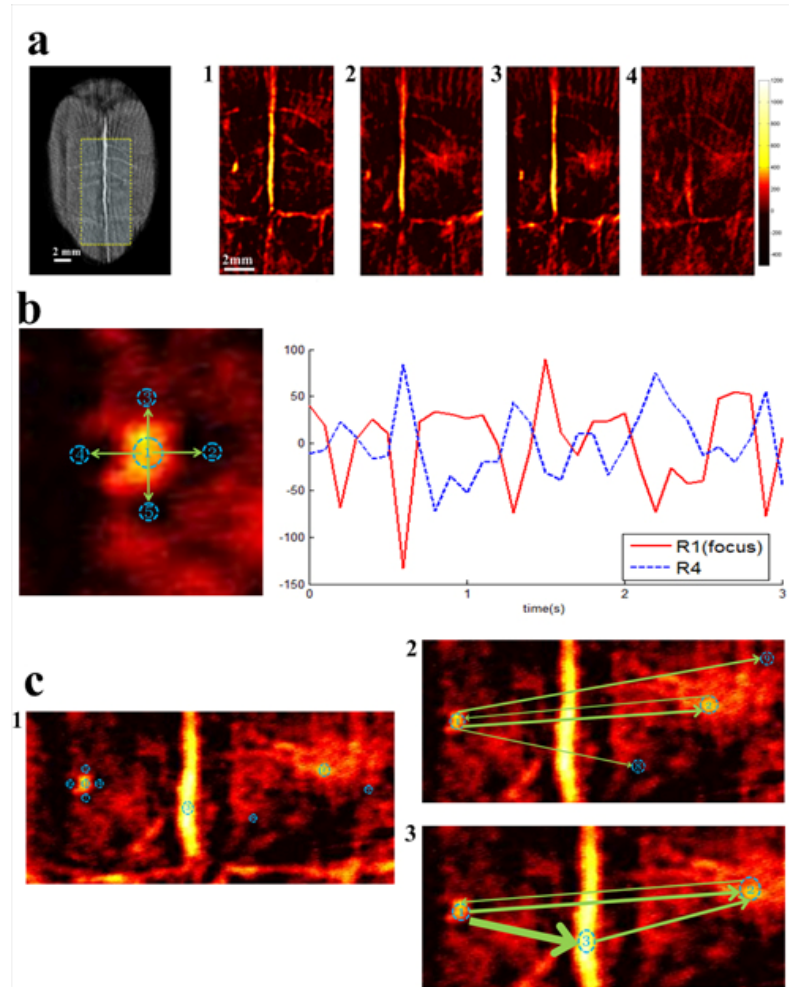
Figure 11 *In vivo* **Maps of contralateral homotopic seizure foci (a)** Left, the PAT image of the rat brain; the yellow dotted rectangular shows the region of interest for analysis; Right, noninvasive imaging of the primary and mirror foci in contralateral homotopic cortex. A1-4 shows how secondary epileptic foci were generated and diminished. The PA signal in the secondary foci was smaller in magnitude and delayed in time compared to the signal recorded from the primary foci. **(b)** Left, Granger analysis of the image around the foci and its immediate secondary foci; Right, PA signal from the foci (red) and secondary area (blue) during an ictal event. **(c)** Pairwise Granger analysis of the seizure foci, contralateral homotopic foci and middle cerebral artery. **C1,** PAT image showing the 9 selected regions of interest; **C2,** Arrows indicate Granger connectivity maps between the primary and secondary foci; **C3,** Connectivity maps between the primary and secondary foci, and the middle cerebral artery.

We also found a spatial temporal correlation between the occurrence of interictal spikes and local blood vessel dynamic changes of the vessel size. **Figure 12a** shows PA image of the rat cortex vasculature through the intact scalp and skull. The red arrow indicates the microvascularity (MV) along the direction marked by the yellow dashed line, representing a cross-sectional scanning using a 50 MHz ultrasound transducer. Positive and negative acoustic peaks induced by a 25 μm blood vessel were sorted out as target signals to track the change of the vessel diameter. Typical PA signals from the targeted vessel at different times show apparent vessel vasomotion by ~40% during the interictal discharges (**Fig. 12b**). Interestingly, the EEG recording (**Fig. 12c**) shows that the interictal spikes had a strong correlation with the

discrete change in vessel size observed photoacoustically (**Fig. 12d**; error bars ± s.d. were calculated from 20 consecutive spikes). Vasomotion during seizure onset and spread was clearly caused by the oscillation in vessel diameter and the expansion of the vessel cross section. We reasoned that the dilation resulted in an active cerebral microvasculature response to increased metabolic activity accompanying the seizure. The combination of multi-scale imaging ability and endogenous hemoglobin contrast makes PAT a promising tool for imaging microvasculature during seizure onset.
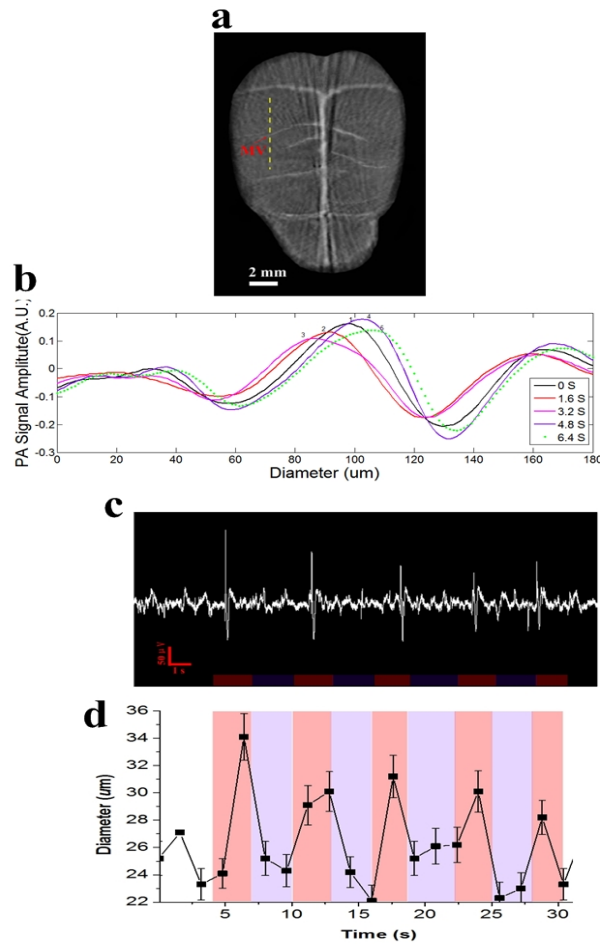

Figure 12 Changes of Blood Vessel Diameter during interictal onset. (a) PA image of the rat cortex vasculature with the intact scalp and skull. The red arrow indicates the microvascularity (MV) along the yellow dashed line direction for a cross-sectional scanning using a 50 MHz ultrasound transducer. **(b)** Typical photoacoustic signals from the targeted vessel at different times. **(c)** EEG recordings show the interictal spikes. **(d)** Change of the vessel size captured by PAT. There was a clear correlation between the interictal spikes and the changes of the vessel size. Error bars (± s.d.) were calculated from 20 consecutive spikes.

Key Research Accomplishments

1. We have developed the advanced boundary conditions scheme, and implemented the 3D reconstruction codes and their parallelization which allowed efficient high performance PAT image reconstruction.
2. We have conducted simulation and phantom experiments that confirmed our software enhancement.
3. We have performed extensive *in vivo* experiments using the rat epilepsy model to evaluate the PAT system we developed in this project. The results show that we were able to image the functional anatomy of epileptic foci noninvasively and in real time at a spatial resolution of ~150µm.

Reportable Outcomes (see the Appendix to this Summary Report)

We have published two journal papers during Year 3. In addition, we expect that the results generated from the simulation, phantom and animal experiments completed in Year 3 will allow us to produce numerous journal publications and conference proceedings in Year 4.

Conclusions

We have made a significant progress that has fulfilled the statement of work proposed for Year 3 of this project. The real-time PAT system completed in Years 1 and 2 has provided us a platform for performing extensive animal experiments. In Year 4 we will focus on animal studies of continuous recording of EEG and PAT over a long period of time to monitor seizure activity continuously to characterize changes during interictal, ictal and post-ictal periods when a spontaneous seizure occurs. We are confident that we will be able to fulfill or exceed the work statement for Year 4.

Appendix

(1) L. Yao, H. Jiang, "Enhanced photoacoustic tomography using total variation minimization", *Applied Optics* **50**, 5031–5041 (2011).

(2) L. Yao and H. Jiang, "Photoacoustic image reconstruction from few-detector and limited-angle data," *Biomed. Opt. Express* **2**, 2649-2654 (2011).

(3) L. Xiang, L. Ji, T. Zhang, B. Wang, J. Yang, Q. Zhang, M. S. Jiang, J. Zhou, P. R. Carney, H. Jiang, "Non-Invasive Real-Time Tomographic Imaging of Epileptic Foci and Networks," *Brain* (submitted).

Enhancing finite element-based photoacoustic tomography using total variation minimization

Lei Yao and Huabei Jiang*

Department of Biomedical Engineering, University of Florida, Gainesville, Florida, 32611USA

*Corresponding author: hjiang@bme.ufl.edu

A total variation minimization (TVM)-based finite element reconstruction algorithm for photoacoustic (PA) tomography is described in this paper. This algorithm is used to enhance the quality of reconstructed PA images with time-domain data. Simulations are conducted where different contrast levels between the target and the background, different noise levels, and different sizes and shapes of the target are studied in a 30 mm diameter circular heterogeneous background. These simulated results show that the quality of the reconstructed images can be improved significantly due to the decreased sensitivity to noise effect when the TVM is included in the reconstruction algorithm. The enhancement is further confirmed using experimental data obtained from several phantom experiments and an *in vivo* animal experiment.   © 2011 Optical Society of America

OCIS codes: 100.2980, 170.3010, 170.5120, 170.6960.

1. Introduction

Photoacoustic tomography (PAT) is an emerging noninvasive imaging technique that combines the merits of high optical contrast and high ultrasound resolution in a single modality [1–3]. In PAT, the Helmholtz-like photoacoustic (PA) wave equation has been commonly used as an accurate model for describing laser-induced acoustic wave propagation in tissue. While analytical reconstruction methods have been used for PA image reconstructions, the finite element method (FEM)-based approach appears to be particularly powerful in this regard [4,5]. The advantages of the FEM-based PAT method include (1) quantitative imaging capability by recovering optical absorption coefficient, (2) elimination of the assumption of homogeneous acoustic medium needed in analytical methods, (3) accommodation of object boundary irregularity, and (4) appropriate boundary conditions implementations.

Our finite element PAT approaches are based on a regularized iterative Newton method, which have been tested and evaluated using extensive simula-tions and phantom experiments in both the frequency and time domain [4–7]. Compared with the frequency domain method, the time domain method can reconstruct images with less background arti-facts, especially when the target size is very small, and can provide a more accurately recovered target size [7]. While these results are encouraging and pro-mising, we realize that measurement noises are still the major factor affecting the quantitative accuracy of the reconstructed images. For example, errors for quantitatively recovering optical absorption coeffi-cient can be as large as 10% for simulated data with 5% noise added and 20% for experimental data [6,7].

In an effort to reduce the noise effect and further enhance the quantitative accuracy of PA image reconstruction, in this paper, we consider a total variation minimization (TVM) scheme within our FEM-based reconstruction framework. Our existing reconstruction algorithms are based on the least-squares criteria (i.e., the regularized Newton meth-od) [8,9] that stand on the statistical argument that the least-squares estimation is the best estimator over an entire ensemble of all possible pictures. Total variation, on the other hand, measures the oscilla-tions of a given function and does not unduly punish

discontinuities [10,11]. Hence, one can hypothesize that a hybrid of these two minimization schemes should be able to provide higher-quality image reconstructions. In fact, the strategy of finding minimal total variation has proved to be successful in applications including electrical-impedance tomography [11], microwave imaging [12], image processing [10,13,14], optimal design [15], and diffuse optical tomography [16]. The TVM has also been implemented and tested in a non-FEM-based PA reconstruction framework [17–19].

In Section 2, we describe in detail the implementation of TVM within our existing PAT reconstruction framework in the time domain. In Section 3, we demonstrate the enhanced reconstruction algorithm using simulated, phantom, and *in vivo* data. The conclusions are made in Section 4

2. TVM Scheme

To describe our TVM method, we first briefly introduce the FEM-based regularized Newton method in the time domain. The time domain PA wave equation in tissue can be described as follows [20]:

$$\nabla^2 p(\mathbf{r}, t) - \frac{1}{v_0^2} \frac{\partial^2 p(\mathbf{r}, t)}{\partial t^2} = -\frac{\Phi(\mathbf{r})\beta}{C_p} \frac{\partial J(t)}{\partial t}, \quad (1)$$

where p is the pressure wave, v_0 is the speed of acoustic wave in the medium, β is the thermal expansion coefficient, C_p is the specific heat, Φ is the absorbed
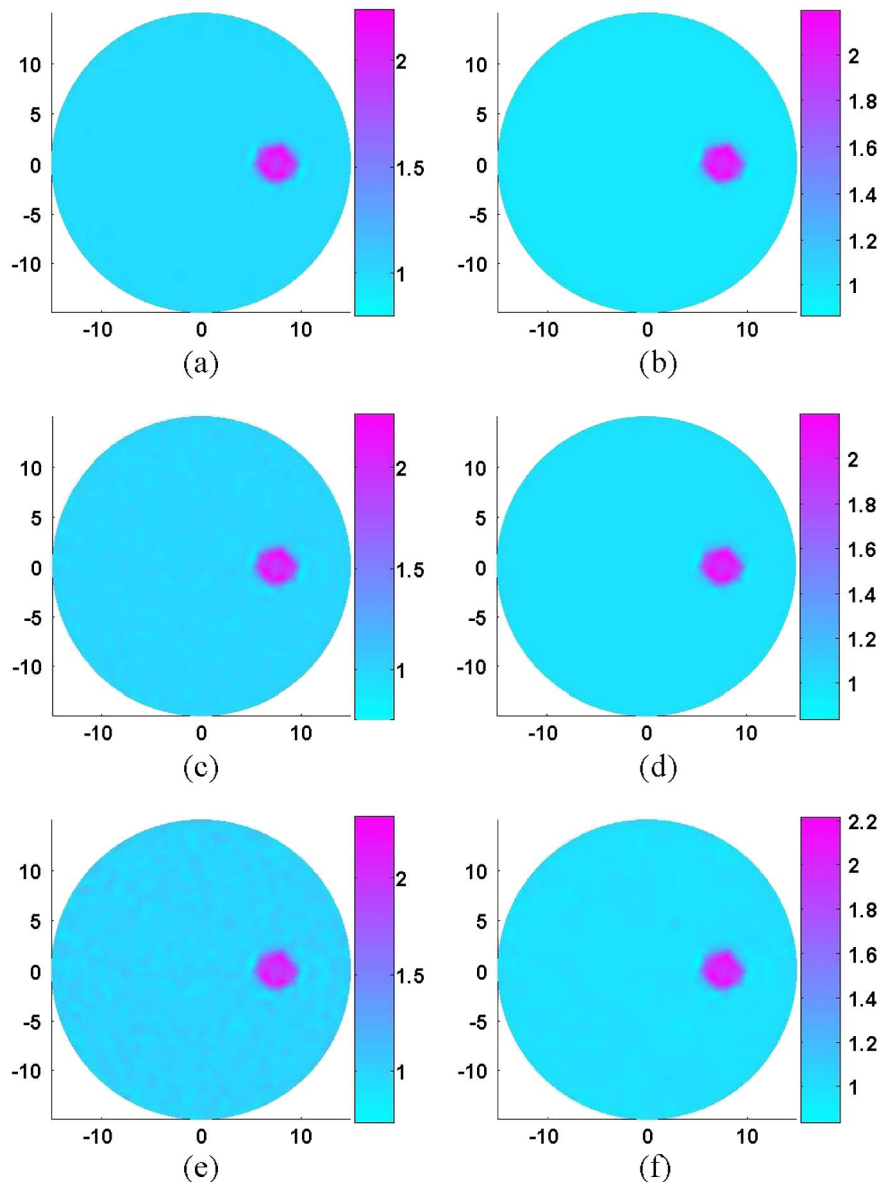

Fig. 1. (Color online) Reconstructed absorbed energy density images from simulated data with and without the TVM enhancement under different noise levels (case 1). (a) Without the TVM, 0% noise, (b) with the TVM, 0% noise, (c) without the TVM, 10% noise, (d) with the TVM, 10% noise, (e) without the TVM, 25% noise, (f) with the TVM, 25% noise. The axes (left and bottom) illustrate the spatial scale in millimeters, whereas the color scale (right) records the absorbed energy density in millijoules per cubed millimeter.

energy density, and $J(t) = \delta(t - t_0)$ is assumed in our study.

Expanding p as the sum of coefficients multiplied by a set of basis function ψ_j, $p = \sum p_j \psi_j$, the finite
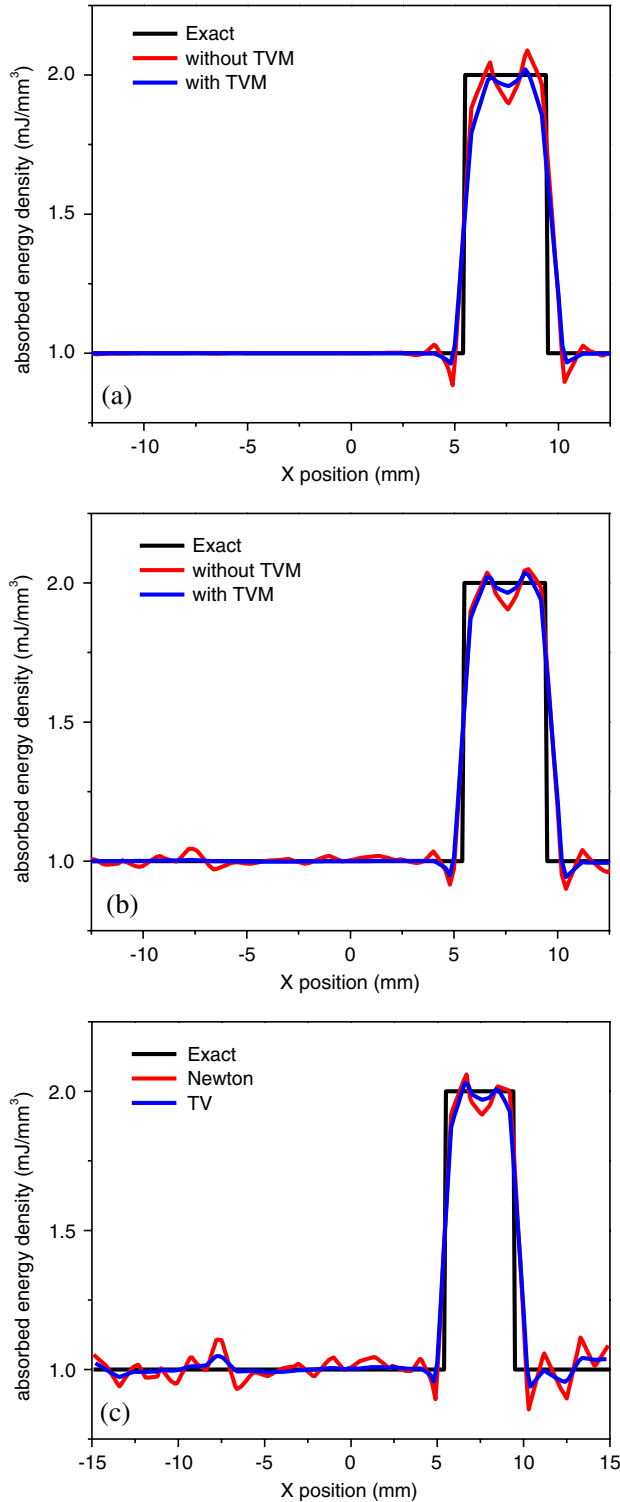

Fig. 2. (Color online) Comparison of the exact and reconstructed absorbed energy density profiles along transect $y = 0$ mm for the images appearing in Fig. 1. (a) 0% noise, (b) 10% noise, (c) 25% noise.

element discretization of Eq. (1) can then be written as [7]

$$\sum_{j=1}^{N} p_j \left[\int_S \nabla \psi_i \cdot \nabla \psi_j \mathrm{d}S \right] + \sum_{j=1}^{N} \ddot{p}_j \left[\int_S \frac{1}{v_0^2} \psi_i \psi_j \mathrm{d}S \right]$$
$$- \oint_l \psi_i \nabla p \cdot \hat{n} \mathrm{d}l = \int_S \frac{\beta \Phi}{C_P} \frac{\partial J}{\partial t} \psi_i \mathrm{d}S. \tag{2}$$

The first-order absorbing boundary conditions used are [21]

$$\nabla p \cdot \hat{n} = -\frac{1}{v_0} \frac{\partial p}{\partial t} - \frac{p}{2r}, \tag{3}$$

where $\hat{n}$ is the unit normal vector.

In both the forward and inverse calculations, the unknown coefficient Φ needs to be expanded in a similar fashion to p as a sum of unknown parameters multiplied by a set of locally spatially varying Lagrange polynomial basis functions. Thus, the matrix form of Eq. (2) becomes

$$[K]\{p\} + [C]\{\dot{p}\} + [M]\{\ddot{p}\} = \{B\}, \tag{4}$$

where the elements of matrix $[K]$, $[C]$, and $[M]$ are

$$K_{ij} = \int_S \nabla \psi_i \cdot \nabla \psi_j \mathrm{d}S + \frac{1}{2r} \oint_l \psi_i \psi_j \mathrm{d}l;$$
$$C_{ij} = \frac{1}{v_0} \oint_l \psi_i \psi_j \mathrm{d}l;$$
$$M_{ij} = \frac{1}{v_0^2} \int_S \psi_i \psi_j \mathrm{d}S;$$

and the column vectors $\{p\}$, $\{\dot{p}\}$, $\{\ddot{p}\}$, and $\{B\}$ are

$$B_i = \frac{\beta}{C_p} \int_S \psi_i \left(\sum_k \psi_k \Phi_k \right) \mathrm{d}S \cdot \frac{\partial J}{\partial t}$$
$$\{p\} = \{p_1, p_2, \cdots p_N\}^T;$$
$$\{\dot{p}\} = \{\dot{p}_1, \dot{p}_2, \cdots \dot{p}_N\}^T;$$
$$\{\ddot{p}\} = \{\ddot{p}_1, \ddot{p}_2, \cdots \ddot{p}_N\}^T.$$

Here, the Newmark's time-stepping scheme has been used for the discretization of time dimension [22,23], which is a commonly used implicit method for the second-order propagation equations such as Eq. (4).

To form an image from a presumably uniform initial guess of the absorbed energy density distribution, we need a method of updating Φ from its starting value. This update is accomplished through the least-squares minimization of the following functional:

$$F(p, \Phi) = \sum_{j=1}^{M} (p_j^0 - p_j^c)^2, \tag{5}$$

where p_j^0 and p_j^c are observed and computed acoustic field data for $j = 1, 2, \cdots M$ boundary locations. Using the regularized Newton method, we obtained the following equation for updating Φ:
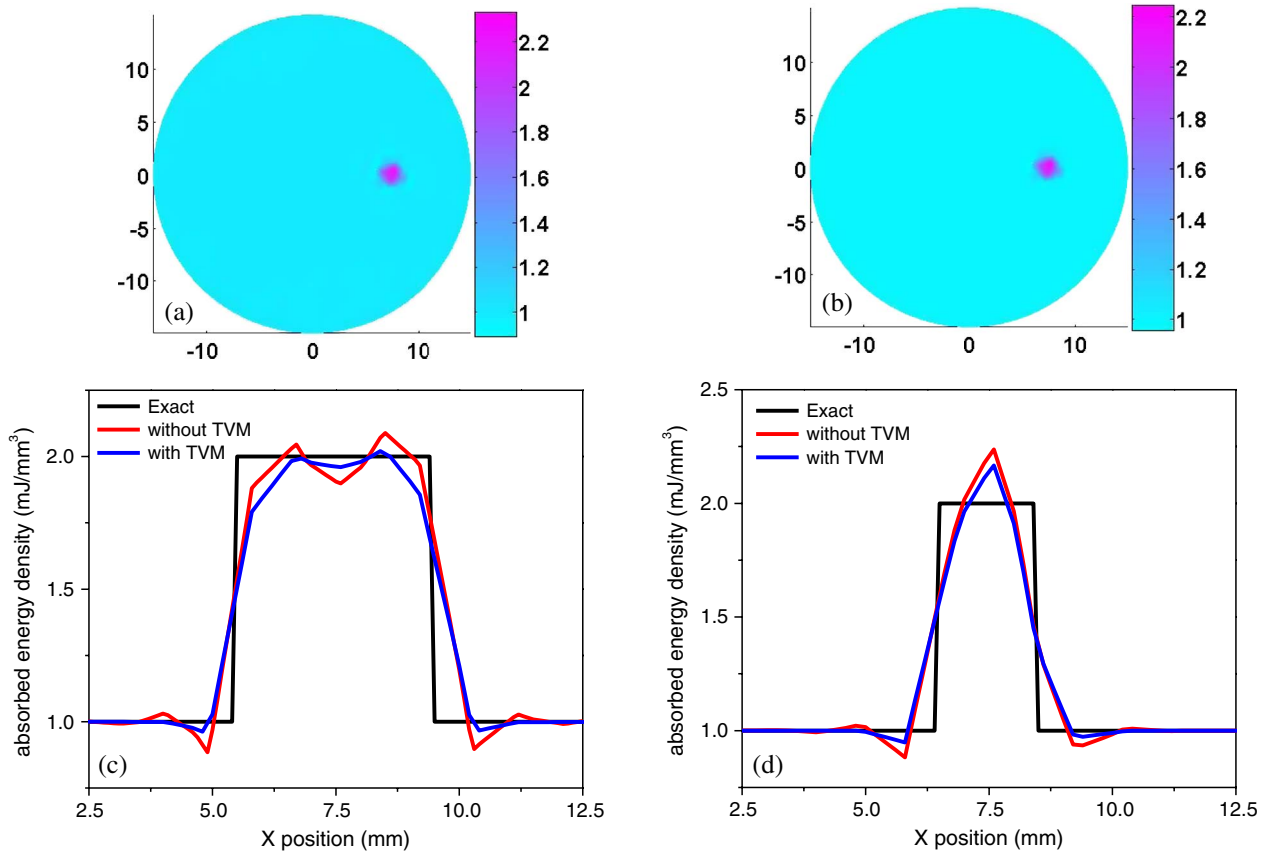
Fig. 3. (Color online) Reconstructed absorbed energy density images from simulated data with and without the TVM enhancement with different target sizes (case 2). (a) Without the TVM, 2 mm diameter target; (b) with the TVM, 2 mm diameter target; (c) absorbed energy density profiles along the transect $y = 0$ mm for the images appearing in Figs. 1(a) and 1(b) (4 mm diameter target); (d) absorbed energy density property profiles along the transect $y = 0$ mm for the images appearing in Figs. 3(a) and 3(b) (2 mm diameter target). In (a) and (b), the axes (left and bottom) illustrate the spatial scale in millimeters, whereas the color scale (right) records the absorbed energy density in millijoules per cubed millimeter.

$$(\mathfrak{I}^T\mathfrak{I} + \lambda\mathbf{I})\Delta\chi = \mathfrak{I}^T(p^0 - p^c), \qquad (6)$$

where $p^0 = (p_1^0, p_2^0, \cdots p_M^0)^T$, $p^c = (p_1^c, p_2^c, \cdots p_M^c)^T$, $\Delta\chi$ is the update vector for the absorbed optical energy density, $\mathfrak{I}$ is the Jacobian matrix formed by $\partial p/\partial\Phi$ at the boundary measurement sites, λ is the regularization parameter determined by combined Marquardt and Tikhonov regularization schemes, and $\mathbf{I}$ is the identity matrix.

Two typical approaches exist for minimizing total variation: a constrained minimization through the solution of the nonlinear PA equation [8,24] and an unconstrained minimization by addition of the total variation as a penalty term to the least-squares functional [10,13,14,25]. From a computational standpoint, unconstrained minimizations are much easier to implement and require fewer modifications to the existing algorithm [13]. Thus, in this study, the unconstrained TVM is used.

We now incorporate the total variation of Φ as a penalty term by defining a new functional [9,10,13]:

$$\tilde{F}(p, \Phi) = F(p, \Phi) + L(\Phi). \qquad (7)$$

Here,

$$L(\Phi) = \int \sqrt{\omega_\Phi^2|\nabla\Phi|^2 + \delta^2}\,\mathrm{d}x\mathrm{d}y \qquad (8)$$

is the penalty term, and ω_Φ and δ are typically positive parameters that need to be determined numerically. The minimization of Eq. (7) proceeds in standard fashion by the differentiation of $\tilde{F}$ with respect to each nodal parameter that constitutes the Φ distribution; simultaneously, all these relations are set to zero. These steps lead to the following nonlinear system of equations

$$\frac{\partial\tilde{F}}{\partial\Phi_i} = -\sum_{j=1}^{M}(p_j^o - p_j^c)\frac{\partial p_j^c}{\partial\Phi_i} + V_i, \qquad (i = 1, 2 \cdots N),$$
$$(9)$$

where

$$V_i = \frac{\partial L}{\partial\Phi_i}$$

$$= \int \frac{\omega_\Phi^2\left[\left(\sum_{k=1}^{N}\Phi_k\frac{\partial\psi_k}{\partial x}\right)\frac{\partial\psi_i}{\partial x} + \left(\sum_{k=1}^{N}\Phi_k\frac{\partial\psi_k}{\partial y}\right)\frac{\partial\psi_i}{\partial y}\right]}{\sqrt{\omega_\Phi^2\left[\left(\sum_{k=1}^{N}\Phi_k\frac{\partial\psi_k}{\partial x}\right)^2 + \left(\sum_{k=1}^{N}\Phi_k\frac{\partial\psi_k}{\partial y}\right)^2\right] + \delta^2}}$$
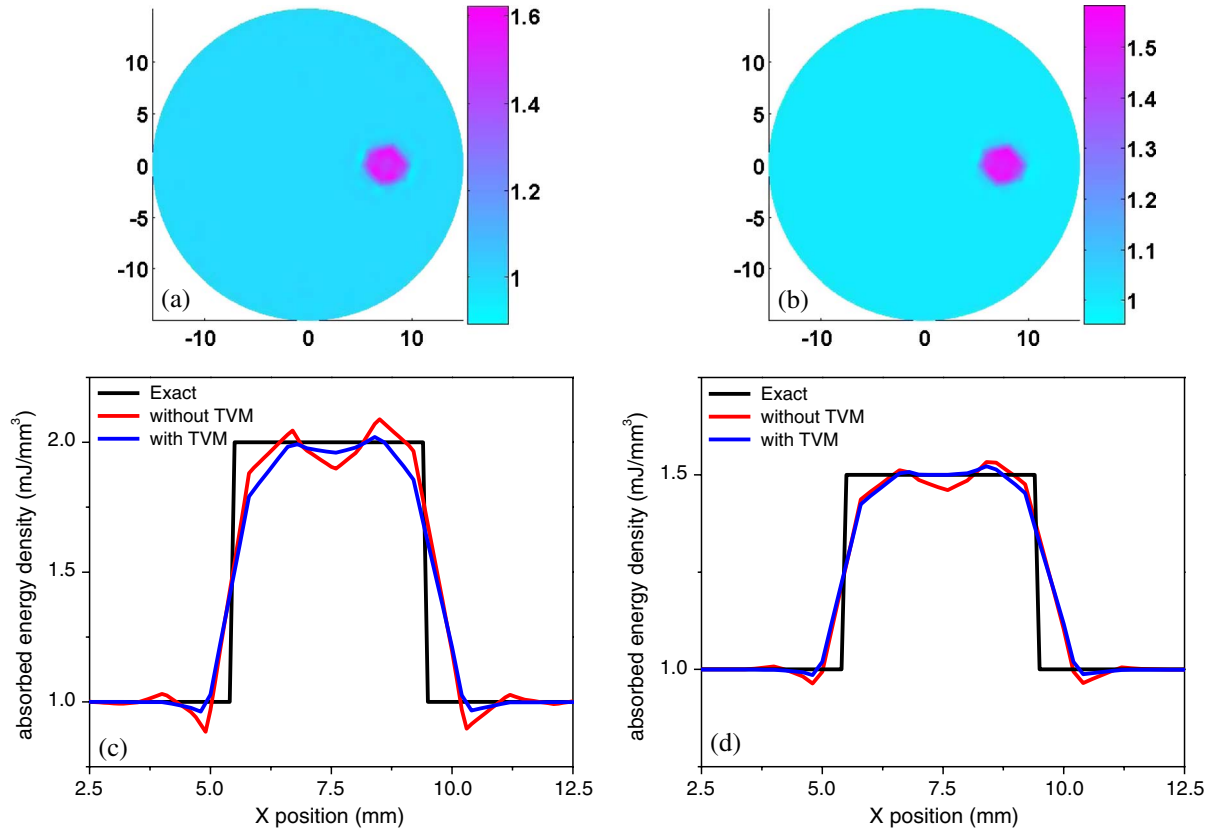$$\times\,\mathrm{d}x\mathrm{d}y.$$

Fig. 4. (Color online) Reconstructed absorbed energy density images from simulated data with and without the TVM enhancement with different contrast levels between the target and the background (case 3). (a) Without the TVM, 1.5∶1 contrast; (b) with the TVM, 1.5∶1 contrast; (c) absorbed energy density profiles along the transect $y = 0\,\mathrm{mm}$ for the images appearing in Figs. 1(a) and 1(b) (2∶1 contrast); (d) absorbed energy density profiles along the transect $y = 0\,\mathrm{mm}$ for the images appearing in Figs. 4(a) and 4(b) (1.5∶1 contrast). In Figs. 4(a) and 4(b), the axes (left and bottom) illustrate the spatial scale in millimeters, whereas the color scale (right) records the absorbed energy density in millijoules per cubed millimeter.

Similar to Eq. (6), the following matrix equation for TVM constrained inversion can be obtained:

$$(\mathfrak{I}^T\mathfrak{I} + R + \lambda I)\Delta\chi = \mathfrak{I}^T(p^0 - p^c) - V, \qquad (10)$$

where

$$R = \begin{bmatrix} \frac{\partial V_1}{\partial\Phi_1} & \frac{\partial V_1}{\partial\Phi_2} & \cdots & \frac{\partial V_1}{\partial\Phi_N} \\ \frac{\partial V_2}{\partial\Phi_1} & \frac{\partial V_2}{\partial\Phi_2} & \cdots & \frac{\partial V_2}{\partial\Phi_N} \\ \cdots & \cdots & \ddots & \\ \vdots & \vdots & \ddots & \\ \frac{\partial V_N}{\partial\Phi_1} & \frac{\partial V_N}{\partial\Phi_2} & \cdots & \frac{\partial V_N}{\partial\Phi_N} \end{bmatrix}$$

and $V = \{V_1, V_2, \cdots V_N\}^T$.

3. Results and Discussion

In this section, the TVM-enhanced reconstruction algorithm is tested and evaluated using both simulated and experimental data. For comparative purposes, reconstructions without the TVM enhancement are also presented.

A. Simulations

In these simulations, a dual-meshing method, as detailed elsewhere [6], is used for fast yet accurate inverse computation. The fine mesh used for the forward calculation consisted of 3627 nodes and 7072 elements, while the coarse mesh used for the inverse calculation had 930 nodes and 1768 elements. All the images obtained from the method without the TVM are the results of three iterations, while those obtained from the TVM-enhanced method are the results of 15 or more iterations. Parallel code was used to perform these calculations on Beowulf clusters with 8 central processing units (CPUs). The computational time can be further reduced if clusters with more than 8 CPUs are used. As mentioned earlier, the parameters ω_Φ and δ were determined through numerical experimentation. A constant value of $\delta = 0.001$ was sufficient for the current simulation and experimental studies, while the value of ω_Φ is related to the signal-to-noise ratio of the measurements [14]. For the simulations presented, $\omega_\Phi = 0.5$ for cases 1, 2, and 3, and $\omega_\Phi = 1.0$ for case 4 was used.

For the first simulation, the test geometry is a 30 mm diameter circular background containing an
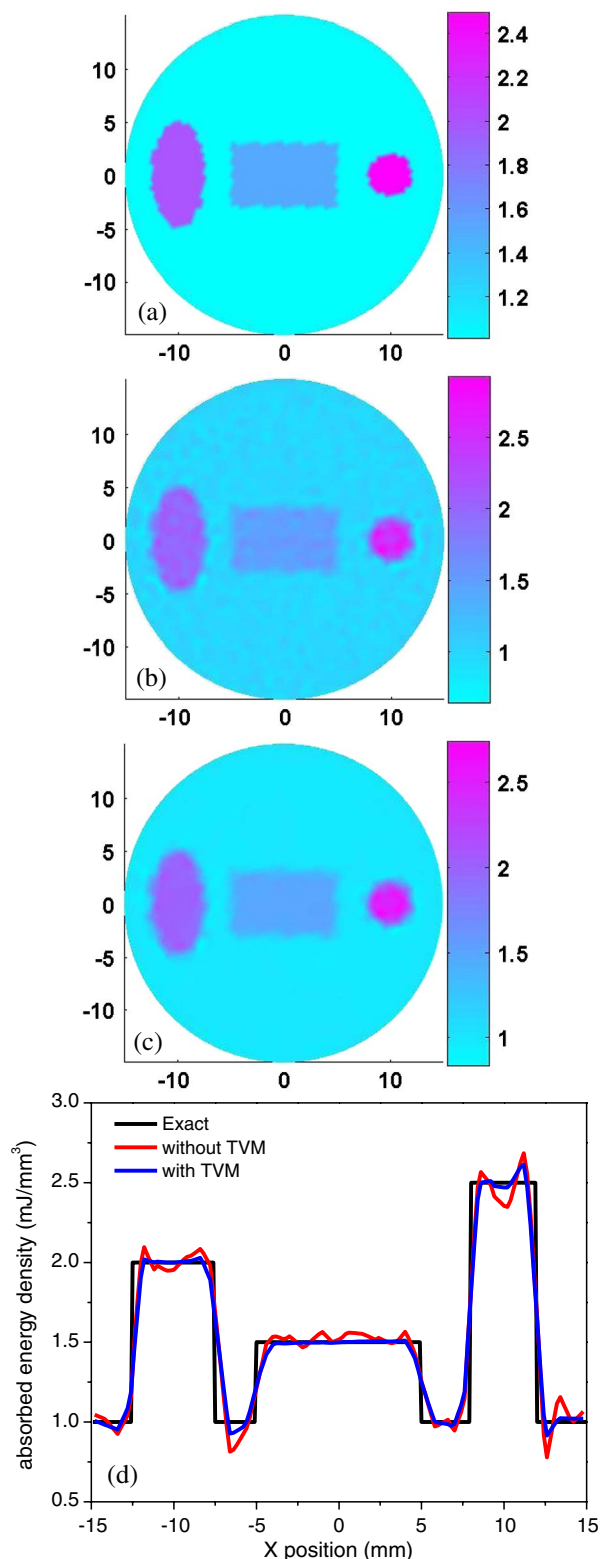
Fig. 5. (Color online) Reconstructed absorbed energy density images from simulated data with and without the TVM enhancement for three targets having different shapes (case 4). (a) Exact image, (b) without the TVM, (c) with the TVM, (d) absorbed energy density profiles along the transect $y = 0\,\text{mm}$. In (a)–(c), the axes (left and bottom) illustrate the spatial scale in millimeters, whereas the color scale (right) records the absorbed energy density in millijoules per cubed millimeter.

off-center 4 mm diameter target region. The target had $\Phi = 2.0\,\text{mJ/mm}^3$, while the background had $\Phi = 1.0\,\text{mJ/mm}^3$. In this case, the image reconstruction was performed with 0%, 10%, and 25% noise added to the "measured" data. Figure 1 gives two sets of absorbed energy density images recovered using the reconstruction method without [Figs. 1(a), 1(c), and 1(e)] and with the TVM enhancement [Figs. 1(b), 1(d), and 1(f)] under the conditions of different noise levels. As can be seen, enhancement of the reconstruction by the incorporation of the TVM is obvious over the method without the TVM. To provide a more quantitative assessment of these images, Fig. 2 is included, in which the reconstructed absorbed energy density profiles are displayed along transects through the target for the images shown in Fig. 1. We find that the TVM-enhanced method not only can improve the quality of the recovered images, but also can decrease the sensitivity of the method to noise effect.

The second simulation is intended to investigate how the target size affects the TVM enhancement. In this case, no noise was added to the "measured" data, and the diameter of the off-center target was 2 mm. Figures 3(a) and 3(b) give two sets of absorbed energy density images recovered using the method without the TVM [Fig. 3(a)] and with the enhancement [Fig. 3(b)], while Figs. 3(c) and 3(d) present the quantitative profiles of the absorbed energy density along transects through the target for the images shown in Figs. 1(a), 1(b), 3(a), and 3(b). Again, considerable improvement can be observed from the reconstructed results when the TVM is invoked compared with the method without the TVM. It is also interesting to note that the enhancement for this case is more striking than that for the first one where the background contained a larger target.

The third simulation aims to see how the contrast level of the absorbed energy density between the target and the background impacts the TVM enhancement. In this case, no noise was added to the "measured" data, and the off-center target had a diameter of 4 mm and $\Phi = 1.5\,\text{mJ/mm}^3$. Figures 4(a) and 4(b) present two sets of absorbed energy density images recovered using the method without the TVM [Fig. 4(a)] and with the TVM enhancement [Fig. 4(b)], while Figs. 4(c) and 4(d) show the quantitative profiles of the absorbed energy density along transects through the target for the images shown in Figs. 1(a), 1(b), 4(a), and 4(b). We can see that the images formed by incorporation of the TVM are clearly enhanced qualitatively in visual content relative to that obtained using the method without the TVM. We also note that lower the contrast level is, the larger the enhancement.

In the fourth simulation, three targets having different shapes (circular, elliptical, and rectangular) were embedded in the background, and the absorbed energy density of these targets was 2.5, 1.5, and $2.0\,\text{mJ/mm}^3$, respectively. A noise level of 25% was added to the "measured" data in this case. Figure 5 shows the exact and the recovered absorbed energy density images as well as the quantitative absorbed
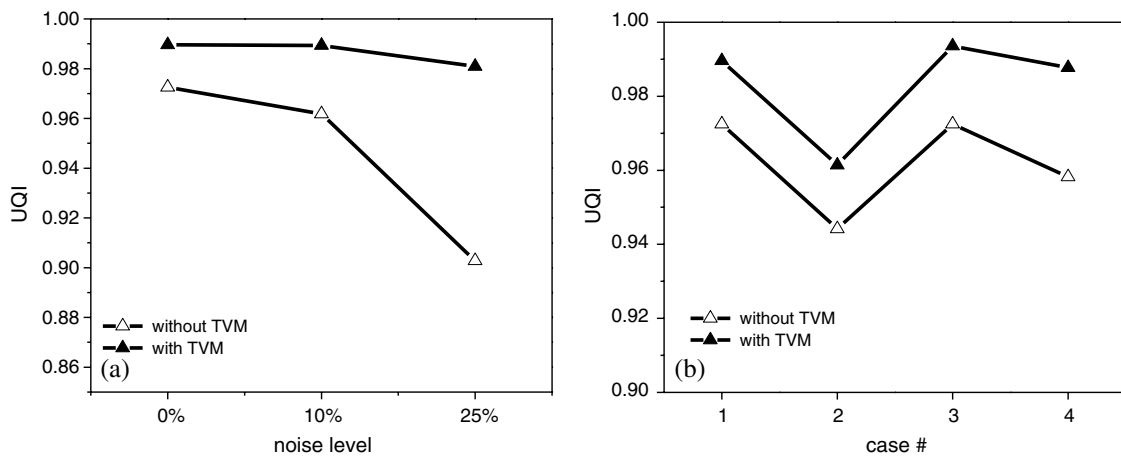
Fig. 6.   UQI calculated from the recovered images with and without TVM enhancement from simulated data. (a) Case 1 when different noise levels are considered, (b) cases 2–4.
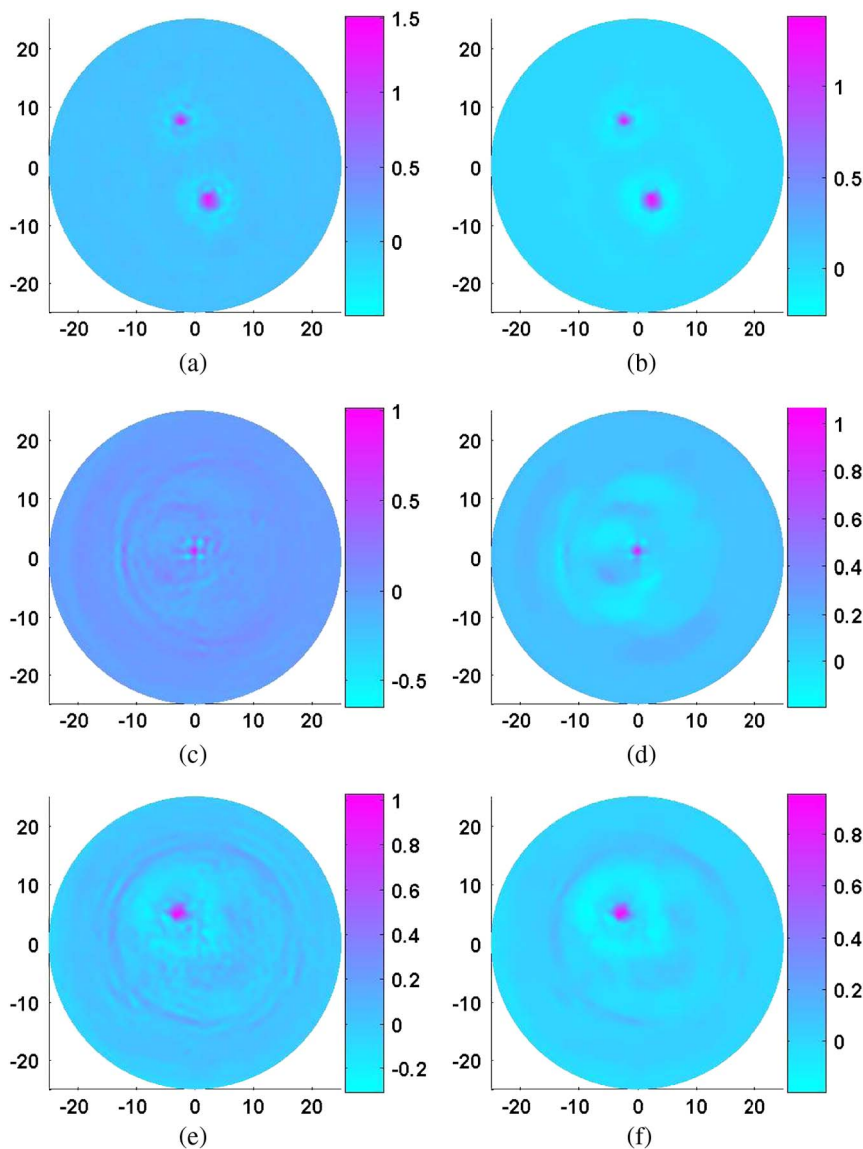

Fig. 7.   (Color online) Reconstructed absorbed energy density images from the three phantom experiments. (a) Case 1 without the TVM, (b) case 1 with the TVM, (c) case 2 without the TVM, (d) case 2 with the TVM, (e) case 3 without the TVM, (f) case 3 with the TVM. The axes (left and bottom) illustrate the spatial scale in millimeters, whereas the color scale (right) records the absorbed energy density in millijoules per cubed millimeter.

energy density property profiles along the transect that across these targets. Again, the improvement in image quality is apparent.

In order to quantitatively evaluate the reconstruction quality using the reconstruction method with and without TVM enhancement, we used the universal quality index (UQI) to measure the degree of similarity between the reconstructed and exact images [26]. We first interpreted an image $\mathbf{f}$ as vectors of size $N : \mathbf{f} = (f_1, f_2, \cdots f_N)^T$, where superscript T denotes the matrix transpose, and N denotes the number of image data acquired from the FEM-based algorithm. We then defined image means, variances and covariances over the whole image domain as

$$\bar{f}^j = \frac{1}{N} \sum_{k=1}^{N} f_k^j, \qquad (11)$$

$$\sigma^j = \sqrt{\frac{1}{N} \sum_{k=1}^{N} (f_k^j - \bar{f}^j)^2}, \qquad (12)$$

where $j = 0$ and 1, and

$$\text{Cov}\{\mathbf{f}^1, \mathbf{f}^0\} = \frac{1}{N} \sum_{k=1}^{N} (f_k^1 - \bar{f}^1)(f_k^0 - \bar{f}^0). \qquad (13)$$

Hence, the UQI is defined as

$$\text{UQI}\{\mathbf{f}^1, \mathbf{f}^0\} = \frac{2\text{Cov}\{\mathbf{f}^1, \mathbf{f}^0\}}{(\sigma^1)^2 + (\sigma^0)^2} \frac{2\bar{f}^1\bar{f}^0}{(\bar{f}^1)^2 + (\bar{f}^0)^2}. \qquad (14)$$

UQI measures the image similarity between the reconstructed ($\mathbf{f}^1$) and reference/exact ($\mathbf{f}^0$) images, and its value ranges between 0 and 1. The value of the UQI is closer to 1 when the reconstructed image is more similar to the exact image. We calculated the UQIs for the simulation cases presented earlier, and the results are given in Fig. 6, where Figs. 6(a) and 6(b) show the UQIs for case 1 when different noise level is considered and for all the four cases without added noise. In Fig. 6, the horizon axis indicates the case number (from cases 1 to 4, presented earlier), and
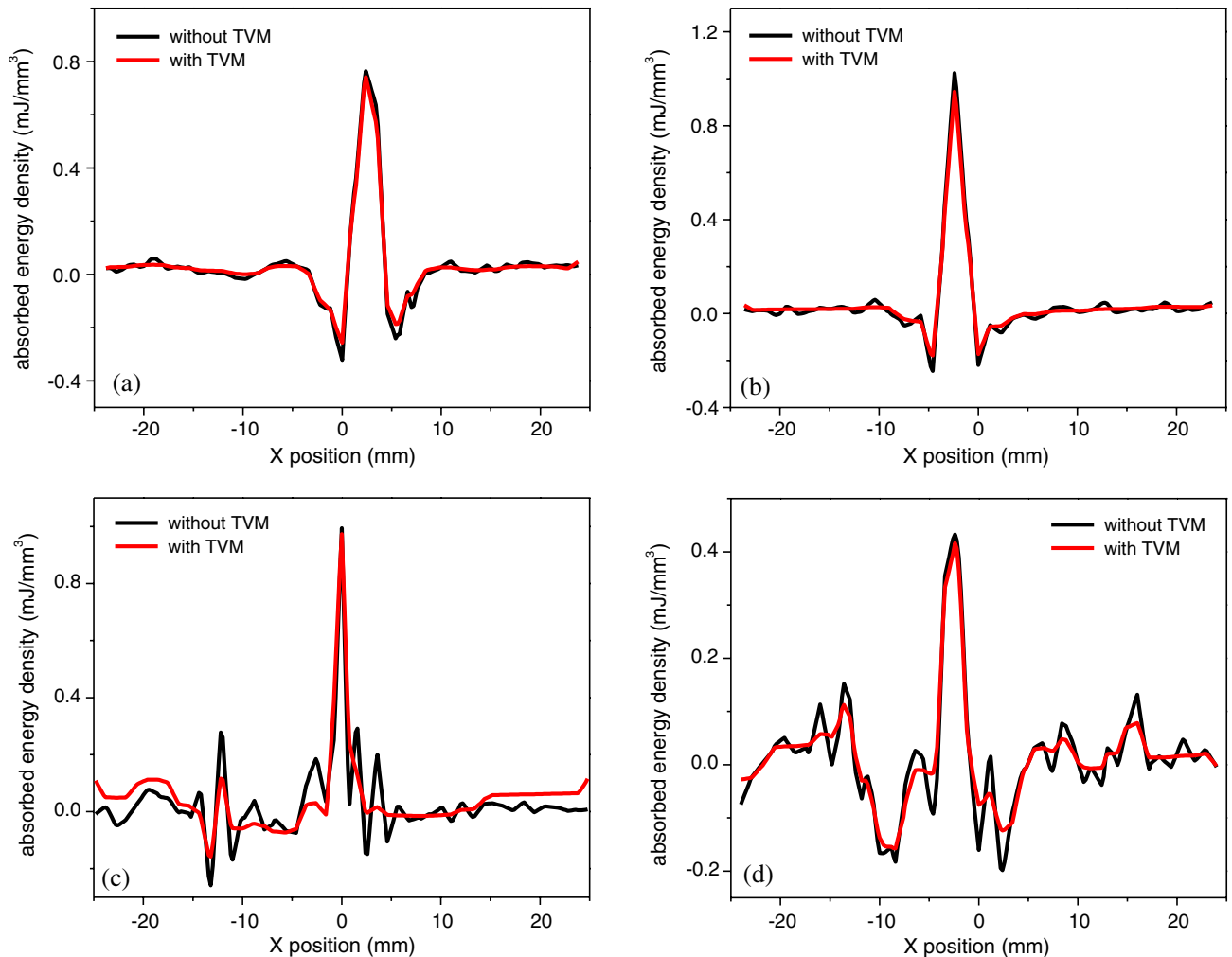

Fig. 8. (Color online) Recovered absorbed energy density profiles along (a) $y = -7.0\,\text{mm}$ crossing the 3 mm diameter target for experimental case 1, (b) $y = 8.0\,\text{mm}$ crossing the 2 mm diameter target for experimental case 1, (c) $y = 1.0\,\text{mm}$ for experimental case 2, and (d) $y = 6.5\,\text{mm}$ for experimental case 3.
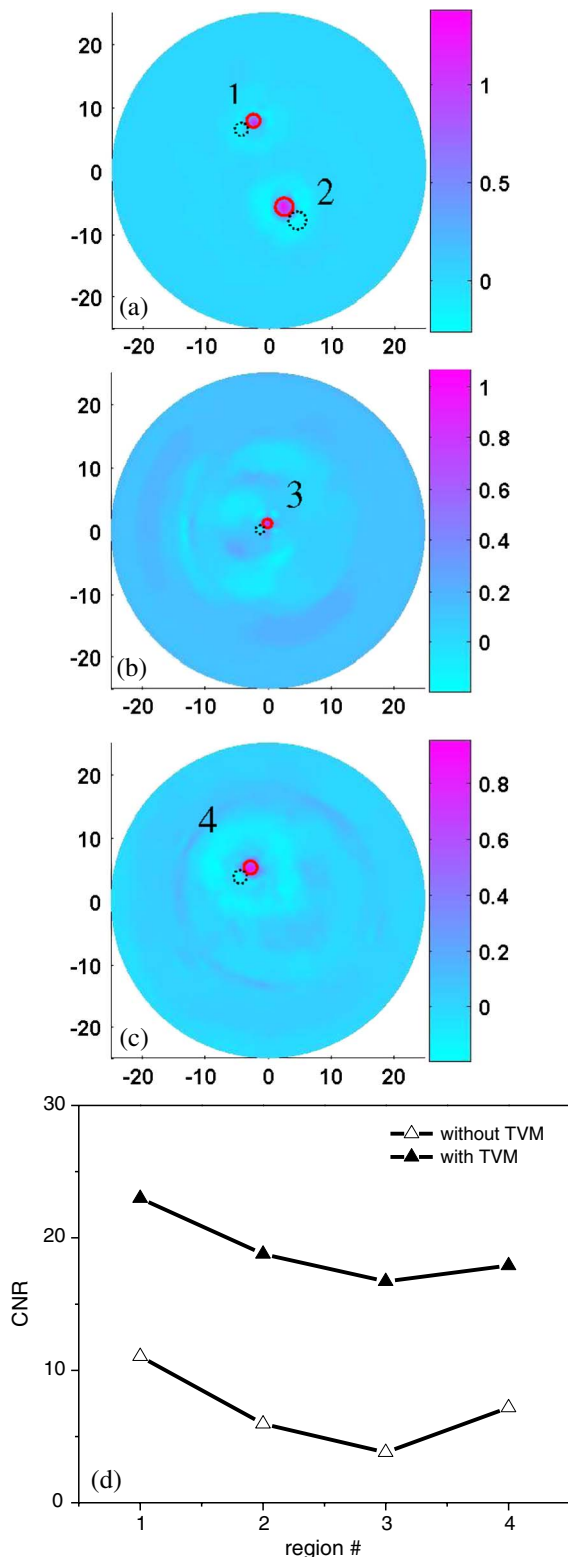
Fig. 9. (Color online) CNR calculated for the recovered images using the method with and without TVM. (a)–(c) Images shown in Figs. 7(b), 7(d), and 7(f) with the ROIs marked (four pairs of ROIs: solid line circle, t-ROI; dashed line circle, b-ROI). (d) CNR computed for the four pairs of ROIs shown in (a)–(c). In Figs. 9 (a)–9(c), the axes (left and bottom) illustrate the spatial scale in millimeters, whereas the color scale (right) records the absorbed energy density in millijoules per cubed millimeter.

the vertical axis shows the value of UQI. We immediately note from Fig. 6 that the TVM-based method provides significantly better UQIs than that without TVM.

B. Phantom and *In Vivo* Experiments

In this section, both phantom and *in vivo* experimental data were used to confirm our findings from the simulations. The experimental setup used for collecting the phantom data was a pulsed Nd:YAG laser-based single transducer (1 MHz) scanning system, which was described in detail elsewhere [5]. Three phantom experiments were conducted. In the first two experiments, we embedded one or two objects with a size ranging from 3 to 0.5 mm in a 50 mm diameter solid cylindrical phantom. The phantom materials used consisted of Intralipid as a scatterer and India ink as an absorber with Agar powder (1%–2%) for solidifying the Intralipid and India ink solution. The absorption coefficient of the background phantom was $0.01\,\text{mm}^{-1}$, while the absorption coefficient of the target(s) was $0.03\,\text{mm}^{-1}$. In the last experiment, we used a single target-containing phantom, aiming to test the capability of detecting targets having low optical contrasts relative to the background phantom. In this case, the target had an absorption coefficient of $0.015\,\text{mm}^{-1}$. The reduced scattering coefficients of the background phantom and targets were 1.0 and $3.0\,\text{mm}^{-1}$ for the first two experiments, and 1.0 and $2.0\,\text{mm}^{-1}$ for the last experiment.

A total of 120 receivers were equally distributed along the surface of the circular background region. In the reconstructions, the fine mesh used for the forward calculation consisted of 5977 nodes and 11,712 elements, while the coarse mesh used for the inverse calculation had 1525 nodes and 2928 elements. The reconstructed images were the results of three and 15 iterations for the method without and with the TVM, respectively. For these experimental cases, $\omega_\Phi = 1.0$ and $\delta = 0.001$ for the cases 1 and 3 and $\omega_\Phi = 2.0$ and $\delta = 0.001$ for case 2 were used.

Here we note that, in the experimental situation, the effect of ultrasonic transducer response should be considered in the PAT image reconstruction because the transducer mechanical–electrical impulse response as well as the transducer aperture effect may introduce significant errors in the forward model. To reduce these effects in our calculations, we applied the normalized acoustic pressure distribution in the reconstruction and used the appropriate parameters (initial values, etc.) obtained from an optimization/searching method [27].

Figure 7 shows the reconstructed absorbed energy density images for all the three experimental cases, while Fig. 8 presents quantitative absorption coefficient profiles along transects through one target for the images shown in Fig. 7. We see that considerably enhanced images are achieved with the TVM, especially when the target is small (case 2), or when the
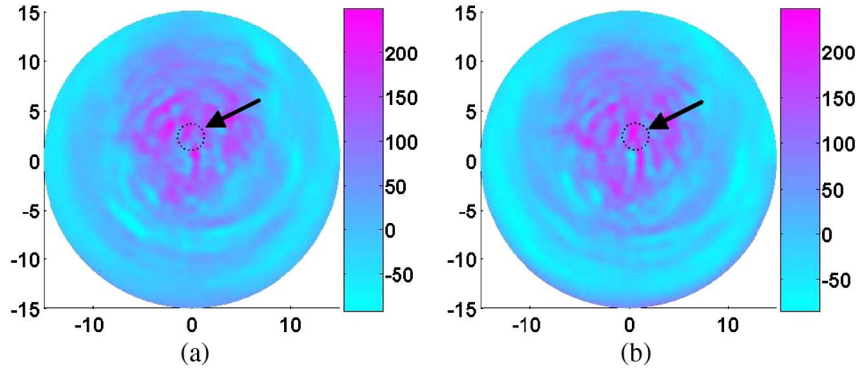
Fig. 10. (Color online) Recovered absorbed energy density images from the rat brain (a) without the TVM, (b) with the TVM. The axes (left and bottom) illustrate the spatial scale in millimeters, whereas the color scale (right) records the absorbed energy density in millijoules per cubed millimeter.

contrast level between the target and the background is low (case 3).

Because there is no true or exact image available for the experimental cases, we used the contrast-to-noise ratio (CNR) to quantitatively evaluate the experimental results. To compute CNR, we selected two regions of interest (ROIs), each having the same size. One region is in the target (referred as t-ROI) and the other is in the background (denoted as b-ROI). The CNR is defined as

$$\text{CNR} = \frac{|\bar{f}^{(t)} - \bar{f}^{(b)}|}{\sigma^{(b)}}, \qquad (15)$$

where $\bar{f}^{(t)}$ and $\bar{f}^{(b)}$, respectively, denote the mean over the t-ROI and b-ROI, and $\sigma^{(b)}$ denotes the variances over the b-ROI. We used solid and dashed circles to express the t-ROI and b-ROI for the three experimental cases. We calculated the CNR for each pair of the t- and b-ROIs using Eq. (15) and present the results in Fig. 9(d). We see that the CNR obtained using the method with TVM is clearly larger than that using the method without TVM, indicating that the TVM-based method is less sensitive to the noise effects.

As a final example, our methods were tested using *in vivo* data collected previously from an animal (rat) model of epilepsy [28]. Focal seizures were induced by microinjection of bicuculline methiodide (BMI) into the parietal neocortex. The *in vivo* data were collected using the same pulsed Nd:YAG laser-based scanning PAT system. In the reconstruction, the fine mesh used for the forward calculation consisted of 17,713 nodes and 34,944 elements, while the coarse mesh used for the inverse calculation had 4489 nodes and 8736 elements. The *in vivo* images obtained were the results of two and five iterations for the methods without and with the TVM, respectively. We found that $\omega_{\Phi} = 0.1$ and $\delta = 0.001$ appeared to provide optimal results.

Figure 10 gives the recovered images for the rat brain scanned 10 min after the injection of BMI without and with the use of the TVM. The *in vivo* results shown here confirm that both of the reconstruction

methods can provide quality images (the arrow indicates the detected seizure focus), while notable enhancement in image quality can be observed with the TVM-based method. For example, the actual continuous middle cerebral artery (indicated by the dashed circle) is shown discontinued in Fig. 10(a) (without the TVM), while this feature is clearly depicted in Fig. 10(b) (with the TVM).

4. Conclusions

We have presented a time-domain FEM-based PA image reconstruction method that incorporates the TVM. The results shown in this work indicate that the TVM-based method is able to offer clear enhancement in image reconstruction over the method without the TVM, not only in terms of the location, size, and shape of the target, but also in terms of the absorbed energy density property/optical absorption coefficient values themselves. In addition, the results have shown that the inclusion of the TVM in our reconstruction algorithm is highly effective in the presence of noisy data. Finally, it is important to note that the TVM-based method may be ideal for image reconstruction involving a low contrast level between the target and the background or small targets embedded in the background.

References

1. G. Paltauf, J. Viator, S. Prahl, and S. Jacques, "Iterative reconstruction algorithm for optoacoustic imaging," J. Acoust. Soc. Am. **112**, 1536–1544 (2002).
2. S. J. Norton and T. Vo-Dinh, "Optoacoustic diffraction tomography: analysis of algorithms," J. Opt. Soc. Am. A **20**, 1859–1866 (2003).
3. A. A. Oraevsky, A. A. Karabutov, S. V. Solomatin, E. V. Savateeva, V. A. Andreev, Z. Gatalica, H. Singh, and R. D. Fleming, "Laser optoacoustic imaging of breast cancer in vivo," Proc. SPIE **4256**, 6–15 (2001).
4. Z. Yuan and H. Jiang, "Quantitative photoacoustic tomography: recovery of optical absorption coefficient maps of heterogenous media," Appl. Phys. Lett. **88**, 231101 (2006).

5. L. Yin, Q. Wang, Q. Zhang, and H. Jiang, "Tomographic imaging of absolute optical absorption coefficient in turbid media using combined photoacoustic and diffusing light measurements," Opt. Lett. **32**, 2556–2558 (2007).

6. H. Jiang, Z. Yuan, and X. Gu, "Spatially varying optical and acoustic property reconstruction using finite-element-based photoacoustic tomography," J. Opt. Soc. Am. A **23**, 878–888 (2006).

7. L. Yao and H. Jiang, "Finite-element-based photoacoustic tomography in time-domain," J. Opt. A **11**, 085301 (2009).

8. K. D. Paulsen and H. Jiang, "Spatially-varying optical property reconstruction using finite element diffusion equation approximation," Med. Phys. **22**, 691–702 (1995).

9. S. R. Arridge, "Forward and inverse problems in time-resolved infrared imaging," in *Medical Optical Tomography: Functional Imaging and Monitoring*, G. J. Mueller, B. Chance, R. R. Alfano, S. B. Arridge, J. Beuthen, E. Gratton, M. Kaschke, B. R. Masters, S. Svanberg, and P. van der Zee, eds., SPIE Institute Series (SPIE, 1993), Vol. IS11, pp. 35–64.

10. D. C. Dobson and F. Santosa, "An image-enhancement technique for electrical impedance tomography," Inverse Probl. **10**, 317–334 (1994).

11. P. M. van den Berg and R. E. Kleinmann, "A total variation enhanced modified gradient algorithm for profile reconstruction," Inverse Probl. **11**, L5–L10 (1995).

12. C. R. Vogel and M. E. Oman, "Iterative methods for total variation denoising," SIAM J. Sci. Comput. **17**, 227–238 (1996).

13. D. C. Dobson and F. Santosa, "Recovery of blocky images from noisy and blurred data," SIAM J. Appl. Math. **56**, 1181–1198 (1996).

14. D. C. Dobson, "Exploiting ill-posedness in the design of diffractive optical structures," Proc. SPIE **1919**, 248–257 (1993).

15. R. Acar and C. R. Vogel, "Analysis of bounded variation penalty methods for ill-posed problems," Inverse Probl. **10**, 1217–1229 (1994).

16. K. D. Paulsen and H. Jiang, "Enhanced frequency-domain optical image reconstruction in tissues through total-variation minimization," Appl. Opt. **35**, 3447–3458 (1996).

17. K. Wang, E. Y. Sidky, M. A. Anastasio, A. A. Oraevsky, and X. Pan, "Limited data image reconstruction in optoacoustic tomography by constrained total variation minimization," Proc. SPIE **7899**, 78993U (2011).

18. J. Provost and F. Lesage, "The application of compressed sensing for photo-acoustic tomography," IEEE Trans. Med. Imaging **28**, 585–594 (2009).

19. Z. Guo, C. Li, L. Song, and L. V. Wang, "Compressed sensing in photoacoustic tomography in vivo," J. Biomed. Opt. **15**, 021311 (2010).

20. A. C. Tam, "Applications of photoacoustic sensing techniques," Rev. Mod. Phys. **58** 381–430 (1986)

21. A. Bayliss and E. Turkel, "Radiation boundary conditions for wave-like equations," Commun. Pure Appl. Math. **33**, 707–725 (1980).

22. I. M. Smith and D. V. Griffiths, *Programming the Finite Element Method* (Wiley, 2004).

23. O. C. Zienkiewicz, R. L. Taylor, and J. Z. Zhu, *Finite Element Method: Its Basis and Fundamentals* (Butterworth, 2005).

24. L. I. Rudin, S. Osher, and E. Fatemi, "Nonlinear total variation based noise removal algorithm," Physica D **60**, 259–268 (1992).

25. S. R. Arridge, P. van der Zee, M. Cope, and D. Delpy, "Reconstruction methods for infrared absorption imaging," Proc. SPIE **1431**, 204–215 (1991).

26. Z. Wang and A. Bovik, "A universal image quality index," IEEE Signal Process. Lett. **9**, 81–84 (2002).

27. N. Iftimia and H. Jiang, "Quantitative optical image reconstruction of turbid media by use of direct-current measurements," Appl. Opt. **39**, 5256–5261 (2000).

28. Q. Zhang, Z. Liu, P. R. Carney, Z. Yuan, H. Chen, S. N. Roper, and H. Jiang, "Non-invasive imaging of epileptic seizures *in vivo* using photoacoustic tomography," Phys. Med. Biol. **53**, 1921–1931 (2008).

Photoacoustic image reconstruction from few-detector and limited-angle data

Lei Yao and Huabei Jiang*

Department of Biomedical Engineering, University of Florida, Gainesville, FL 32611, USA
*hjiang@bme.ufl.edu

Abstract: Photoacoustic tomography (PAT) is an emerging non-invasive imaging technique with great potential for a wide range of biomedical imaging applications. However, the conventional PAT reconstruction algorithms often provide distorted images with strong artifacts in cases when the signals are collected from few measurements or over an aperture that does not enclose the object. In this work, we present a total-variation-minimization (TVM) enhanced iterative reconstruction algorithm that can provide excellent photoacoustic image reconstruction from few-detector and limited-angle data. The enhancement is confirmed and evaluated using several phantom experiments.

OCIS codes: (100.2980) Image enhancement; (170.3010) Image reconstruction techniques; (170.5120) Photoacoustic imaging; (170.6960) Tomography

References and links

1. G. Paltauf, J. A. Viator, S. A. Prahl, and S. L. Jacques, "Iterative reconstruction algorithm for optoacoustic imaging," J. Acoust. Soc. Am. **112**(4), 1536–1544 (2002).
2. S. J. Norton and T. Vo-Dinh, "Optoacoustic diffraction tomography: analysis of algorithms," J. Opt. Soc. Am. A **20**(10), 1859–1866 (2003).
3. A. A. Oraevsky, A. A. Karabutov, S. V. Solomatin, E. V. Savateeva, V. A. Andreev, Z. Gatalica, H. Singh, and R. D. Fleming, "Laser optoacoustic imaging of breast cancer in vivo," Proc. SPIE **4256**, 6–15 (2001).
4. L. A. Kunyansky, "Explicit inversion formulae for the spherical mean radon transform," Inverse Probl. **23**(1), 373–383 (2007).
5. D. Finch, S. Patch, and Rakesh, "Determining a Function from Its Mean Values Over a Family of Spheres," SIAM J. Math. Anal. **35**(5), 1213–1240 (2004).
6. M. Xu and L. V. Wang, "Universal back-projection algorithm for photoacoustic computed tomography," Phys. Rev. E Stat. Nonlin. Soft Matter Phys. **71**(1), 016706 (2005).
7. Z. Yuan and H. Jiang, "Quantitative photoacoustic tomography: Recovery of optical absorption coefficient maps of heterogenous media," Appl. Phys. Lett. **88**(23), 231101 (2006).
8. L. Yin, Q. Wang, Q. Zhang, and H. Jiang, "Tomographic imaging of absolute optical absorption coefficient in turbid media using combined photoacoustic and diffusing light measurements," Opt. Lett. **32**(17), 2556–2558 (2007).
9. K. D. Paulsen and H. Jiang, "Spatially varying optical property reconstruction using a finite element diffusion equation approximation," Med. Phys. **22**(6), 691–701 (1995).
10. S. R. Arridge, "Forward and inverse problems in time-resolved infrared imaging," in *Medical Optical Tomography: Functional Imaging and Monitoring*, G. J. Mueller, B. Chance, R. R. Alfano, S. B. Arridge, J. Beuthen, E. Gratton, M. Kaschke, B. R. Masters, S. Svanberg, and P. van der Zee, eds. (SPIE Press, 1993), pp. 35–64.
11. S. J. LaRoque, E. Y. Sidky, and X. Pan, "Accurate image reconstruction from few-views and limited-angle data in diffraction tomography," J. Opt. Soc. Am. A **25**(7), 1772–1782 (2008).
12. J. Bian, J. H. Siewerdsen, X. Han, E. Y. Sidky, J. L. Prince, C. A. Pelizzari, and X. Pan, "Evaluation of sparse-view reconstruction from flat-panel-detector cone-beam CT," Phys. Med. Biol. **55**(22), 6575–6599 (2010).
13. H. Ammari, E. Bretin, V. Jugnon, and A. Wahab, "Photo-acoustic imaging for attenuating acoustic media," in *Mathematical Modeling in Biomedical Imaging II*, H. Ammari, ed., Vol. 2035 of Lecture Notes in Mathematics (Springer, 2011), pp. 53–80.
14. H. Ammari, E. Bossy, V. Jugnon, and H. Kang, "Mathematical models in photoacoustic imaging of small absorbers," SIAM Rev. **52**(4), 677–695 (2010).
15. H. Ammari, E. Bossy, V. Jugnon, and H. Kang, "Reconstruction of the optical absorption coefficient of a small absorber from the absorbed energy density," SIAM J. Appl. Math. **71**, 676–693 (2011).

16. K. Wang, E. Y. Sidky, M. A. Anastasio, A. A. Oraevsky, and X. Pan, "Limited data image reconstruction in optoacoustic tomography by constrained total variation minimization," Proc. SPIE **7899**, 78993U, 78993U-6 (2011).
17. L. Yao and H. Jiang, "Finite-element-based photoacoustic tomography in time-domain," J. Opt. A, Pure Appl. Opt. **11**(8), 085301 (2009).
18. K. D. Paulsen and H. Jiang, "Enhanced frequency-domain optical image reconstruction in tissues through total-variation minimization," Appl. Opt. **35**(19), 3447–3458 (1996).
19. H. Jiang, Z. Yuan, and X. Gu, "Spatially varying optical and acoustic property reconstruction using finite-element-based photoacoustic tomography," J. Opt. Soc. Am. A **23**(4), 878–888 (2006).
20. Z. Wang and A. C. Bovik, "A universal image quality index," IEEE Signal Process. Lett. **9**(3), 81–84 (2002).

1. Introduction

Photoacoustic tomography (PAT) is an emerging non-invasive imaging technique that combines the merits of high optical contrast and high ultrasound resolution in a single modality [1–3]. In PAT, the Helmholtz-like photoacoustic wave equation has been commonly used as an accurate model for describing laser-induced acoustic wave propagation in tissue. While a variety of analytic PAT reconstruction algorithms have been developed [4–6], the finite element method (FEM) based approach appears to be particularly powerful in this regard, because it can provide quantitative imaging capability by recovering optical absorption coefficient [7,8], eliminate the assumption of homogeneous acoustic medium needed in analytical methods, accommodate object boundary irregularity and allow appropriate boundary conditions implementations.

A practical need exists for reconstruction of photoacoustic images from few measurements, as this can greatly reduce the required scanning time and the number of ultrasound sensors placed near or on the boundary of an object to receive the laser-induced acoustic signals. In addition, in many practical implementations of PAT the photoacoustic signals are recorded over an aperture that does not enclose the object, which results in a limited-angle tomographic reconstruction problem. In such cases, the existing reconstruction algorithms, which are based on the least-squares criteria (i.e., the regularized Newton method) [9,10], often generate distorted images with severe artifacts. Total-variation-minimization (TVM), on the other hand, has proved to be a powerful tool for limited-data image reconstruction in diffraction tomography and computed tomography (CT) [11,12]. TVM based PAT algorithms have also been implemented and tested using numerically simulated limited-view data [13–16]. Here we describe an unconstrained TVM FEM-based iterative reconstruction algorithm, and for the first time present experimental evidence that the TVM-based algorithm offers excellent photoacoustic image reconstruction from few-detector and limited-angle data.

This paper is organized as follows. In Section 2, the FEM based PAT reconstruction algorithm and the unconstrained TVM scheme are reviewed briefly. The experimental validation of our TVM FEM-based algorithm is presented in Section 3. The conclusions are made in Section 4.

2. Method

We first briefly describe the existing FEM-based photoacoustic reconstruction algorithm detailed elsewhere [17]. The time-domain photoacoustic wave equation in tissue can be described as follows:

$$\nabla^2 p(\mathbf{r},t) - \frac{1}{v_0^2}\frac{\partial^2 p(\mathbf{r},t)}{\partial t^2} = -\frac{\Phi(\mathbf{r})\beta}{C_p}\frac{\partial J(t)}{\partial t},\qquad(1)$$

where p is the pressure wave; v_0 is the speed of acoustic wave in the medium; β is the thermal expansion coefficient; C_p is the specific heat; Φ is the absorbed energy density; $J(t) = \delta(t - t_0)$ is assumed in our study.

To form an image from a presumably uniform initial guess of the absorbed energy density distribution, we need a method of updating Φ, the desired quantity from its starting value. This update is accomplished through the least-squares minimization of the following functional:

$$F(p,\Phi) = \sum_{j=1}^{M}\left(p_j^0 - p_j^c\right)^2, \qquad (2)$$

where p_j^o and p_j^c are the measured and computed acoustic field data for $i = 1, 2, \cdots M$ boundary locations. Using the regularized Newton method, we obtained the following matrix equation for updating Φ:

$$\left(\Im^T\Im + \lambda\mathbf{I}\right)\Delta\chi = \Im^T\left(p^o - p^c\right), \qquad (3)$$

where $p^0 = \left(p_1^0, p_2^0, \cdots p_M^0\right)^T$ and $p^c = \left(p_1^c, p_2^c, \cdots p_M^c\right)^T$; $\Delta\chi$ is the update vector for the absorbed optical energy density; $\Im$ is the Jacobian matrix formed by $\partial p/\partial\Phi$ at the boundary measurement sites; λ is the regularization parameter determined by combined Marquardt and Tikhonov regularization schemes; and $\mathbf{I}$ is the identity matrix.

We now incorporate the total variation of Φ as a penalty term by defining a new functional [18]:

$$\tilde{F}(p,\Phi) = F(p,\Phi) + L(\Phi). \qquad (4)$$

Here $L(\Phi) = \int\sqrt{\omega_\Phi^2\left|\nabla\Phi\right|^2 + \delta^2}\,dxdy$ is the penalty term, and ω_Φ and δ are typically positive parameters that need to be determined numerically. The minimization of Eq. (4) can be realized by the differentiation of $\tilde{F}$ with respect to each nodal parameter that constitutes the Φ distribution and by setting each of the resulting expression to zero, leading to the following system of equations:

$$\frac{\partial\tilde{F}}{\partial\Phi_i} = -\sum_{j=1}^{M}\left(p_j^o - p_j^c\right)\frac{\partial p_j^c}{\partial\Phi_i} + V_i = 0 \quad (i = 1, 2\cdots N), \qquad (5)$$

where $V_i = \partial L/\partial\Phi_i$. Again, through the regularized Newton method, the following matrix equation for TVM-based inversion is obtained [18]:

$$\left(\Im^T\Im + R + \lambda I\right)\Delta\chi = \Im^T\left(p^0 - p^c\right) - V, \qquad (6)$$

where V is formed by $\partial L/\partial\Phi$ and R is formed by $\partial V/\partial\Phi$. At this point, our solution procedure for solving Eq. (6) and the regularization parameter selection are identical to those described previously. Hence, it becomes clear that the only additions to our new algorithm result from the assembly of matrix R and the construction of column vector V.

3. Results

In this section our TVM enhanced reconstruction algorithm is tested and evaluated using phantom experimental data. For comparative purposes, reconstruction results without the TVM enhancement are also presented.

The experimental setup used for collecting the phantom data was a pulsed ND: YAG laser based single transducer (1MHz) scanning system, which was described in detail elsewhere [8]. Three phantom experiments were conducted. In the first two experiments, we embedded one or two objects with a size ranging from 3 to 0.5 mm in a 50 mm-diameter solid cylindrical phantom. The absorption coefficient of the background phantom was 0.01 mm^{-1}, while the

absorption coefficient of the target(s) was 0.03 mm^{-1}. In the last experiment, we used a single-target-containing phantom, aiming to test the capability of detecting target having low optical contrasts relative to the background phantom. In this case, the target had an absorption coefficient of 0.015 mm^{-1}. The reduced scattering coefficients of the background phantom and targets were 1.0 and 3.0 mm^{-1} for the first two experiments, and 1.0 and 2.0 mm^{-1} for the last experiment. In the reconstructions, we used a dual-meshing scheme [19] where the fine mesh used for the forward calculation consisted of 5977 nodes and 11712 elements, while the coarse mesh used for the inverse calculation had 1525 nodes and 2928 elements. All the images obtained from the method without the TVM are the results of three iterations, while those obtained from the TVM-enhanced method are the results of twenty or more iterations. Parallel code was used to speed up these calculations on Beowulf clusters with 8 CPUs. The computational speed can be further increased if clusters with more than 8 CPUs are used. As mentioned above, the parameters ω_Φ and δ were determined through numerical experimentation. From our experience, a constant value of $\delta = 0.001$ was sufficient for the current experimental studies, while the value of ω_Φ is related to the signal-to-noise ratio of the measurements. For our experimental cases, $\omega_\Phi = 1.0$ and $\delta = 0.001$ for the first case, and $\omega_\Phi = 0.5$ and $\delta = 0.001$ for the second and third cases were used.

The reconstruction results based on few-detector data from the three experimental cases are shown in Figs. 1, 2 and 3, respectively. In each figure, the images in the top and bottom rows, respectively, present the recovered absorbed energy density images using the algorithm without and with the TVM where 120, 60, 30, and 15 detectors were equally distributed along the surface of the circular background region. As expected, the conventional algorithm without the TVM provides high quality images only when the number of detectors was relatively sufficient (Figs. 1a,b, Figs. 2a,b, and Figs. 3a,b). The images reconstructed from few-detector data by the conventional algorithm without the TVM contained severe artifacts and distortions (Figs. 1c,d, Figs. 2c,d, and Figs. 3c,d). Considerably enhanced images are achieved using the method with the TVM, especially when the number of the detectors is reduced to 30 or 15 (Figs. 1g,h, Figs. 2g,h, and Figs. 3g,h). We also note that the computational efficiency of our TVM based algorithm for recovering a small absorber (Fig. 2) and a larger absorber (Fig. 3) is similar when the number of the detectors is insufficient.

Images reconstructed from the limited-angle data for the first case using the two methods are displayed in Fig. 4 where the top and bottom rows, respectively, show the recovered absorbed energy density images using the algorithm without and with the TVM when 120 detectors over 360°, 60 detectors over 180°, and 30 detectors over 90°, were equally
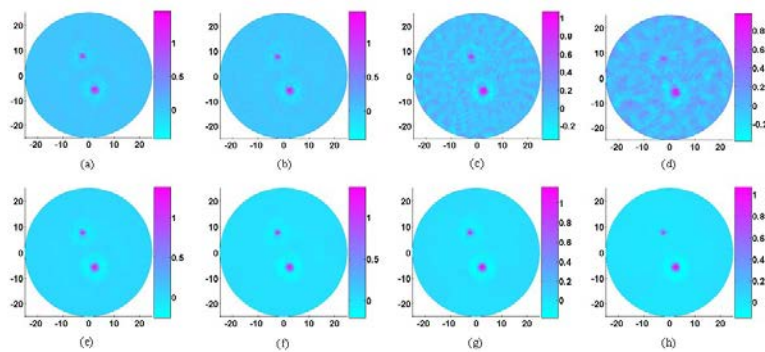

Fig. 1. Reconstructed photoacoustic images based on few-detector data for case 1. (a), 120 detectors, without TVM. (b), 60 detectors, without TVM. (c), 30 detectors, without TVM. (d), 15 detectors, without TVM. (e), 120 detectors, with TVM. (f), 60 detectors, with TVM. (g), 30 detectors, with TVM. (h), 15 detectors, with TVM.
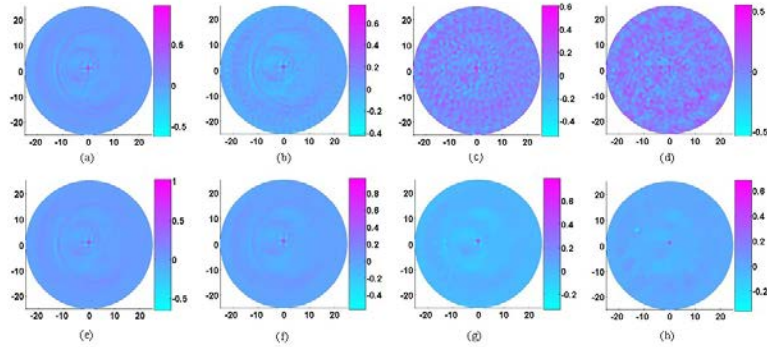
Fig. 2. Reconstructed photoacoustic images based on few-detector data for case 2. (a), 120 detectors, without TVM. (b), 60 detectors, without TVM. (c), 30 detectors, without TVM. (d), 15 detectors, without TVM. (e), 120 detectors, with TVM. (f), 60 detectors, with TVM. (g), 30 detectors, with TVM. (h), 15 detectors, with TVM.
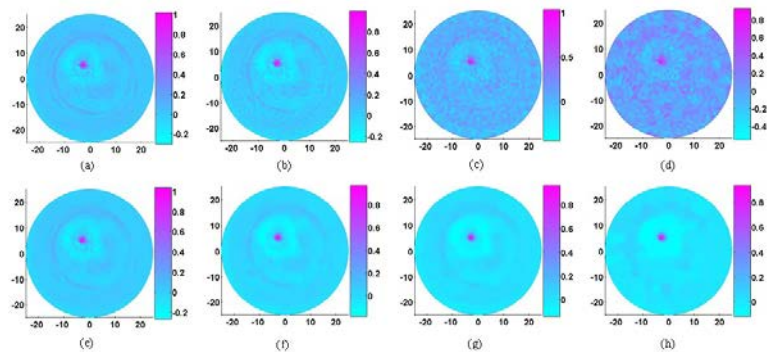

Fig. 3. Reconstructed photoacoustic images based on few-detector data for case 3. (a), 120 detectors, without TVM. (b), 60 detectors, without TVM. (c), 30 detectors, without TVM. (d), 15 detectors, without TVM. (e), 120 detectors, with TVM. (f), 60 detectors, with TVM. (g), 30 detectors, with TVM. (h), 15 detectors, with TVM.
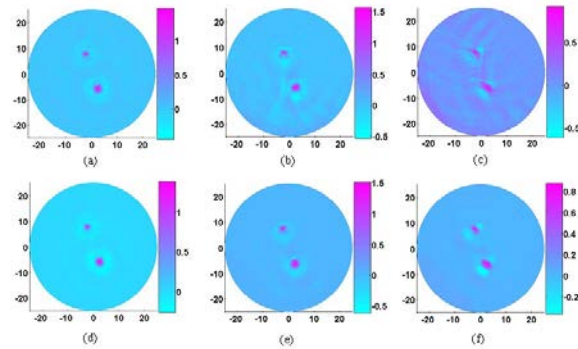

Fig. 4. Reconstructed photoacoustic images based on limited-angle data for case 1. (a), 120 detectors over 360°, without TVM. (b), 60 detectors over 180°, without TVM. (c), 30 detectors over 90°, without TVM. (d), 120 detectors over 360°, with TVM. (e), 60 detectors over 180°, with TVM. (f), 30 detectors over 90°, with TVM.

distributed along the surface of the circular background region. Again, strong artifacts and distortions exist in the images recovered with the method without the TVM when the data collected is angle-limited (Figs. 4b,c), while considerably improved images are reconstructed using the TVM enhanced algorithm (Figs. 4e,f).

In order to evaluate quantitatively the reconstruction quality using the method with and without TVM enhancement, we use the following universal quality index (UQI) [20]:

$$UQI\{\mathbf{f}^1, \mathbf{f}^0\} = \frac{2Cov\{\mathbf{f}^1, \mathbf{f}^0\}}{\left(\sigma^1\right)^2 + \left(\sigma^0\right)^2} \frac{2\overline{f}^1 \overline{f}^0}{\left(\overline{f}^1\right)^2 + \left(\overline{f}^0\right)^2}. \tag{7}$$

Here the image f can be interpreted as vectors of size N: $\mathbf{f} = \left(f_1, f_2, \cdots f_N\right)^T$, where N denotes the number of image data acquired from the FEM based algorithm. $\overline{f}^j$ is the image means, σ^j is the variances, and $Cov\{\mathbf{f}^1, \mathbf{f}^0\}$ is the covariances over the whole image domain, where j = 0 and 1. UQI measures the image similarity between the reconstructed ($\mathbf{f}^1$) and reference ($\mathbf{f}^0$) images, and its value ranges between 0 and 1. The value of the UQI is closer to 1 when the reconstructed image is more similar to the reference image.

We calculated the UQIs for the three cases presented above, and the results are given in Fig. 5 where Figs. 5a and 5b show the results from the few-detector data based on the method without and with the TVM, respectively, while Fig. 5c presents the results from the limited-angle data for the first case based on the two methods. Here the image data recovered by 120 detectors was regarded as the reference one. The computed UQIs shown in Fig. 5 confirm the observation that the TVM enhanced PAT algorithm provides significantly better image quality compared to the conventional method without the TVM.
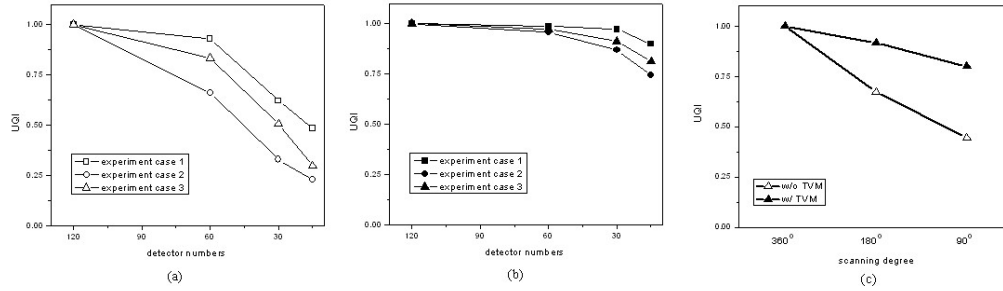

Fig. 5. UQIs calculated from the recovered images for the three cases based on few-detector data without TVM (a) and with TVM (b), and for case 1 based on limited angle data with and without TVM.

4. Conclusions

In this work, we have implemented and evaluated an unconstrained, total-variation-minimization method for time-domain FEM based PAT. This study has confirmed that in the situation that the data is collected from few measurements or over an aperture that does not enclose the object, the developed TVM based PAT algorithm provides considerably improved image reconstruction compared to the conventional methods. The application of this TVM enhanced reconstruction algorithm will significantly reduce the number of ultrasound transducers and scanning time needed for high quality photoacoustic image reconstruction.

Non-Invasive Real-Time Tomographic Imaging of Epileptic Foci and Networks

Liangzhong Xiang,[1] Lijun Ji,[1] Tao Zhang,[1] Bo Wang,[1] Jianjun Yang,[1] Qizhi Zhang,[1] Max S. Jiang,[1] Junli Zhou,[2,3] Paul R. Carney,[1-4], Huabei Jiang[1,*]

[1]J. Crayton Pruitt Family Department of Biomedical Engineering

[2]Departments of Pediatrics, Neurology, and Neuroscience

[3]Wilder Center of Excellence for Epilepsy Research, [4]McKnight Brain Institute

University of Florida

Gainesville, FL 32611, U.S.A.

Total number of words: 4208

Article type: Original research

*Correspondence to: Huabei Jiang, Ph.D.

Tel: +1-352-273-9336**,** E-mail: hjiang@bme.ufl.edu

ABSTRACT

While brain imaging and electrophysiology independently play a central role in today's neuroscience and in the evaluation of neurological disorders, a single noninvasive modality that offers both high spatial and temporal resolution at centimeter scale depths is currently not available. Here we show in an acute epilepsy rat model that photoacoustic tomography (PAT) can noninvasively track seizure brain dynamics with both high spatial and temporal resolution, and at a depth that is clinically relevant. The noninvasive yet whole surface and depth capabilities of the photoacoustic imaging system allowed for the first time to actually see what is happening during ictogenesis in terms of seizure onset and spread. Both seizure onset and propagation were tomographically detected at a spatial resolution of 150 μm and a temporal resolution of 300 ms, respectively. The networks associated with the epileptiform events were identified using Granger Causality, which lend support to the theory that seizure onset and spread involves a rich interplay between multiple cortical and subcortical foci during the onset and spread of focal epilepsy. Dynamical changes of vasculature during epileptiform events were also detected with high spatiotemporal resolution. Together, these findings suggest that PAT represents a powerful tool for noninvasively mapping seizure onset and propagation patterns, and the 'functional' connectivity within epileptic brain networks.

Keywords: neuroimaging; epilepsy; localization; neural networks; microvasculature

Abbreviations: PAT=photoacoustic tomography; EEG= electroencephalography;

BMI= Bicuculline methiodide influences; ROI=region of interest

INTRODUCTION

Epilepsy is a common, chronic, neurological disorder characterized by seizures. Three percent of people will be diagnosed with epilepsy at some time in their lives (Hauser and Kurland 1975, Hauser 1992). Indeed, approximately 50 million people worldwide have epilepsy, and 20 to 30 percent of these patients are refractory to all forms of medical treatment (Hauser 1992) . Seizures are transient signs and symptoms of abnormal, excessive, or hypersynchronous neuronal activity in the brain (Fisher et al. 2005). In most cases, seizures are controlled, although not cured, with anticonvulsant medication. Seizure types are classified according to whether the source of the seizure is localized (partial or focal onset seizures) or distributed (generalized seizures) (Greenfield 2011). Localization-related epilepsies arise from an epileptic focus. A partial seizure may spread within the brain, a process known as secondary generalization. Generalized epilepsies, in contrast, arise from many independent foci (multifocal epilepsies) or from epileptic circuits that involve the whole brain. In epilepsies of unknown localization, it remains unclear as to whether they arise from a portion of the brain or from more widespread circuits.

For those patients with medically intractable focal epilepsy, the best treatment option is resective brain surgery (Birbeck et al. 2002, Duncan et al. 2006, Berg et al. 2007). Although several factors can impact the success of epilepsy surgery, the primary reason of failure is the incomplete mapping of the local epilepsy network which results in incomplete resection of epileptogenic foci (Engel 2004, Jeha et al. 2007). Much of the attention on epilepsy surgery has been directed at identifying single neuronal populations. This approach has, in many cases, led to failed surgical outcomes, because seizures typically involve groups of neurons interacting both locally and across several cortical and subcortical brain regions. A better understanding of the regional interactions occurring at the site of seizure onset and spread

may provide important insights about the pathophysiology of seizures and aid with accurate brain mapping and resection of the epileptic focus.

The epileptic focus is defined as the portion of the brain that serves as the irritant, driving the epileptic response. The seizure focus is generally considered as the place where a seizure starts and the target for surgical intervention. The common belief is that the seizure starts the same way, and that the entire focus acts in unison. In theory, removing the focus should result in a patient's seizures being cured. However, there is much evidence to suggest that the focus is more of a region of seizure onset with a number of sites that can act independently to initiate seizures (Thom et al. 2010). Seizures in animal models and in people often have a multifocal or broadly synchronized onset. The best evidence for multifocality within the seizure onset zone comes from surgical experience with intracranial monitoring. The challenge of mapping the epileptic focus stems from the observation that the pathology associated with focal epilepsy is often distributed across a number of brain sites (Bertram 2009) and that current diagnostics methods frequently fall short of identifying such sites. Animal studies indicate that the neurons involved in the epileptic circuitry have enhanced excitability throughout (Bertram et al. 1998, Fountain et al. 1998, Mangan et al. 2000). The implication of these observations is that each of the sites could act independently to initiate a seizure or, potentially, to drive another site into a seizure. Thus, in focal epilepsy, one may view a cortical region as a broad seizure onset zone, with the potential that multiple foci can act as a seizure focus for any given seizure.

Much of our understanding about focal seizure circuitry comes from electrophysiological recording methods. Although electrophysiology is currently the 'gold standard' in mapping the epileptic focus, it is often inadequate to define the boundary of the epilepsy circuitry due to spatial sampling limitations and volume conduction. What we truly desire is a brain mapping modality, which could give a high-resolution real time spatial and

temporal 'read out' of the dynamics of cortical processing and seizures. It has been well established that optical contrast is highly sensitive to neuronal activity (Hill and Keynes 1949, Grinvald et al. 1988). The high optical contrast is largely due to the changes in blood volume and blood oxygenation. When used intraoperatively, optical imaging or intrinsic optical signal provided excellent surface maps of epileptic focus (Haglund et al. 1992, Haglund and Hochman 2004). Near-infrared spectroscopy has also been used to obtain cerebral blood volume and blood oxygenation in epilepsy patients (Steinhoff et al. 1996, Sokol et al. 2000, Watanabe et al. 2000). However, the major limitation of Near-infrared spectroscopy and or intrinsic optical signa is that each provides only surface depth information. Greater depth information can be obtained by using tomographic reconstruction methods such as diffuse optical tomography (Oleary et al. 1995, Jiang et al. 1996, Bluestone et al. 2001, Boas et al. 2001). Whereas diffuse optical tomography has low spatial resolution, laser-induced photoacoustic tomography (PAT) has both superior spatial and temporal resolution. PAT detects absorbed photons ultrasonically by employing the photoacoustic effect. It combines both high contrast and spectroscopic specificity based on the optical absorption of both oxy- and deoxy-hemoglobin with high ultrasonic spatial resolution (Kruger and Liu 1994, Laufer et al. 2007, Xiang et al. 2007, Yuan et al. 2007). Relative to other optical imaging modalities, PAT has the advantage of mitigating both scalp and skull light scattering by a factor of ~1,000. The end result is that PAT allows for high spatial resolution imaging of brain at a depth considerably beyond the soft depth limit of conventional optical imaging techniques such as confocal microscopy (Sipkins et al. 2005), two-photon microscopy (Denk et al. 1990), and optical coherence tomography (Huang et al. 1991).

In this study, PAT was employed to image seizures in an experimental acute bicuculline methiodide model of focal epilepsy. Bicuculline is a light-sensitive competitive antagonist of

GABA$_A$ receptors that mimics focal epilepsy when applied to brain tissue. During focal application of bicuculline into the brain cortex, brains were imaged noninvasively with a novel PAT system that has three orders of magnitude higher temporal resolution and four-fold higher spatial resolution relative to our previous PAT prototype(Zhang et al. 2008). The high spatiotemporal properties of this PAT imaging tool allowed for identification of both bicuculline elicited focal seizure onset and spread. Off-line, we employed measures of brain connectivity to further identify the functional anatomy implicated in focal cortical seizures. The high spatial and temporal sampling of the novel PAT system allowed for the first time the complete mapping of an epileptiform event *in vivo*. It is also the first report of mapping an epileptiform event at depths well below the cortex. These findings build onto the collection of advantages of noninvasive PAT in brain dynamics and epilepsy. Information from this study can be applied to improve our understanding of epileptic networks and mapping in epilepsy. In terms of impact, this is the first demonstration of a potentially clinical useful adjunct in the clinical surgical evaluation of cortical epilepsy.

MATERIALS AND METHODS

Animals

Male Sprague-Dawley rats (Harlan Labs, Indianapolis, IN) weighing 50-60 g on arrival were allowed one week to acclimate to the 12-h light/dark cycle and given food and water ad libitum. All procedures were approved by the University of Florida Animal Care and Use Committee and conducted in accordance with the National Institutes of Health Guide for the Care and Use of Experimental Animals.

Electrode implantation surgery

Animals were anesthetized intraperitoneally with 1 g/kg of body weight dose of urethane. Two 300 μm diameter stainless steel screw electrodes were implanted within the

skull for obtaining subdural multichannel cortical local field potentials data (−0.3 mm posterior, 3 mm lateral (right) of bregma, 1 mm ventral) based on coordinates from a rat brain atlas(Paxinos 1998). One, 300 μm diameter stainless steel screw electrode (FHC, Bowdoin, ME) was implanted as a reference electrode into the midline occipital bone. Cortical local field potentials were obtained using a Tucker Davis Pentusa (Tucker Davis Technologies, Alachua, FL) neural recording system at 12 kHz, digitized with 16 bits of resolution, and band pass filtered from 0.5 to 6 kHz.

Induction of seizures

Rats (n=10) received 10 μl of 1.9 mM bicuculline methiodide influences (BMI) and 10 μl normal saline into the left and right parietal cortex, respectively. The infusion was performed through the previously implanted electrode sites at a rate of 0.3 μL/min. The infusion system consisted of a 100 μL gas-tight syringe (Hamilton, Reno, NV) driven by a syringe pump (Cole-Parmer, Vernon Hills, IL) connected to polyaryletheretherketone (PEEK) tubing (ID = 0.381mm, OD= 0.794mm, length<0.5 m, Upchurch Scientific, Oak Harbor, WA). The PEEK tubing was coupled to a silica cannula (ID = 50 μm, OD= 147 μm, Polymicro Technologies, Phoenix, AZ) via a microfluidic connector. Cortical local field potentials were recorded 5 min before each injection and continued for up to 30 min thereafter.

Image analysis

A custom software utility was written and incorporated into the computer software package MATLAB (MathWorks, Massachusetts, USA) to analyze and display recorded data. This software enabled the reconstruction of the PAT images and the determination of the blood vessel diameter. Amira (version 5.3.3, TGS Template Graphics Software) was used for three-dimensional reconstruction of the seizure foci. In connectivity analysis, the time series

data were selected from 200 sets of PAT images sampled at 3Hz within the seizure onset period, and at each time point, we chose 9 (regions of interest) ROI (R1~R9) and then the PA signal was averaged within each ROI, as shown in Fig. $4c_1$. Changes in photoacoustic signals were quantified as $-\Delta A/A$ in Fig. 4b, right. The PA data shown in Figs. 2-5 were not averaged. The image color scale was determined by the photoacoustic signal intensity in arbitrary units (between 0 to 1).

RESULTS

PAT imaging

Light from a Ti: Sapphire laser tunable (690 to 950 nm) was delivered through the skull to the brain through an optical fiber (Fig. 1a). The energy of each laser pulse was detected by a photodiode for calibration. A 192 element full-ring transducer array was used to capture the photoacoustic (PA) signals generated by the laser light. The 192 channel data acquisition system consisted of preamplifiers, secondary stage amplifiers (for optimizing the signal-to-noise ratio), and a 3:1 electronic multiplexer coupled with a 64-channel analog-to-digital converter. The estimated PAT data acquisition system speed was 0.33 s/frame. Data acquisition speed was limited in part by the 10 Hz laser repetition (supplemental figure 1, Movie S3). The spatial resolution of the PAT system was inversely related to the bandwidth of the ultrasonic transducer. Each ultrasonic detector had a 5-MHz central frequency and a 70% nominal bandwidth with a diameter of 6mm (Blatek, Inc., PA, U.S.A.). The noninvasive PAT image of the rat cortical vasculature (Fig. 1b) matched well with an anatomical photograph (Fig. 1c) obtained after the PA imaging. The brain structures including the middle cerebral artery, right hemispheres, left hemispheres, left olfactory bulbs, and right olfactory bulbs are clearly shown in the PAT image. Numbers 1-5

marked in the image indicate that the micro-blood vessels with a diameter of less than 100μm are also seen, which again correspond well with the rat brain photograph. This allowed for imaging objects of 50μm in diameter with a spatial resolution of 150μm (supplemental figure 2).

Thirty minutes following the microelectrode placement, PAT imaging was performed to generate baseline tissue absorption maps, visualize micro blood vessels, and morphological cortical landmarks (Figs 2b, c). Subsequently, rats (n=10) received 10 μl of 1.9 mM bicuculline methiodide and 10 μl normal saline into the left [-1.0AP, 2.5ML, 2.4DV] and right [-1.0AP, 2.5 ML, 0.4DV] parietal cortex, respectively, based on coordinates from a rat brain atlas (Paxinos 1998). Immediately following the focal infusions, PAT imaging was repeated to visualize changes in the injection site tissue absorption. An increase in tissue absorption was observed in the bicuculline methiodide cortical injection site and surrounding region (Fig. 2c, left), but not in the saline injection site or surrounding region (Fig. 2c, right). PAT scanning for subcortical changes was also performed. Slices 5, 7, and 9 (Fig. 2d) are the images obtained 3, 5 and 7 mm below the scalp, respectively. Fig. 2e is the three dimensional rendering of the epileptic foci obtained from different tomographic layers (movie S1). Each image exhibited the variable patterns of seizure onset and propagation both at the cortical and subcortical regions. Seizures were confirmed by concomitant time-locked PAT/video-electroencephalography (Fig. 2a). Experiments were repeated for each animal at 2-hour intervals.

Real-time monitoring of epileptic events

Epileptiform events were recorded with PAT from a focal region of interest of ~2 × 3 mm (Fig. 3a). We observed a significant optical absorption change directly associated with de-oxygenation at a wavelength of 755 nm (Fig. 3c). Furthermore, at the seizure onset at

1min 6.267 s, the seizure focus measured 0.2053 mm^2 and increased to 0.5004 mm^2 as the electrographic seizure time-series increased in frequency and amplitude (Fig. 3b). Corresponding rate changes (0.33 s) spike and wave discharges and PA images were observed in each experimental trial. The seizure onset dynamics captured photoacoustically are best appreciated in movies displaying how the seizure was generated and varied over time (movie S2). PAT images suggest that in addition to ictal spread from the primary focus, homotopic foci are seen in the contralateral parietal cortex (Fig. 4a$_{1-4}$). The PA signal in the contralateral foci was smaller in magnitude and delayed in time compared to the signal recorded from the primary seizure foci. We also observed a region of inverted optical signal immediately surrounding the seizure onset zone (Fig 4b, left). We performed analysis of the optical signal at a distance of at least 2 mm away from the edge of the focus. Our results demonstrate that the inverse optical signal was inversely related to the optical signal recorded from the focus (Fig. 4b, right).

To evaluate the dynamic interactions within the seizure circuitry and capture the associated networks we used the frequency domain Granger causality (Brovelli et al. 2004, Granger 1969, Wang et al. 2007) . PAT time series data was selected from 200 sets of PAT images sampled at 3 Hz within the seizure onset period. At each time point we chose 9 ROIs (Fig. 4c$_1$) and used the averaged optical absorption within each region for the network analysis. Nine sets of time series analysis were classified into 3 groups including the primary ictal onset area and corresponding 4 surrounding regions of interest including the primary or initiating seizure focus, contralateral homotopic foci, and 2 regions of interest surrounding the primary focus in the contralateral cortex. The middle cerebral artery, primary seizure focus, and secondary homotopic seizure focus were also analyzed. Results from group 1 analysis demonstrate the causal influence from the primary focus to the surrounding regions of interest (Fig. 4b, left). The negative zero-lag correlation (-0.68) between both the primary

and secondary foci showed that neural activities within these two regions changed in opposite direction over time. We postulate that the inverted change in optical signal was likely due to the opposite oxygen delivery or blood flow(Schwartz and Bonhoeffer 2001). Figure $4c_2$ shows the Granger causality analysis for group 2 data where we see that the primary and secondary contralateral brain foci influenced each other mutually with a stronger influence of the primary focus relative to the contralateral focus. Moreover, we suggest that the primary seizure focus may influence the contralateral foci as previously suggested using optical intrinsic imaging in epilepsy (Khalilov et al. 2003) and microelectrode recordings of hippocampus local field potentials(Zhou et al. 2009, Cadotte et al. 2010). Finally, from group 3 analyses (Fig. $4c_3$) we found that the primary focus strongly influenced the hemodynamic change in the middle cerebral artery, which in turn showed influence on the contralateral homotopic foci.

Dynamical changes of vasculature during interictal discharges

Fig. 5a shows image of the rat cortex vasculature through the intact scalp and skull. The red arrow indicates the microvascularity along the direction marked by the yellow dashed line, representing a cross-sectional scanning using a 50 MHz ultrasound transducer. Positive and negative acoustic peaks induced by a 25 μm blood vessel were sorted out as target signals to track the change of the vessel diameter. Typical PA signals from the targeted vessel at different times show apparent vessel vasomotion by ~40% during the interictal discharges (Fig. 5b). Local field potential recordings (Fig. 5c) showed that interictal spikes had a strong correlation with the discrete change in vessel size observed photoacoustically (Fig. 5d; error bars ± s.d. were calculated from 20 consecutive spikes).

DISCUSSION

The main finding is that PAT imaging is a powerful tool for noninvasively mapping seizure dynamics with both high spatial and temporal resolution. This study investigated the hemodynamic changes during focal seizure onset and propagation in an acute model of focal epilepsy. The experimental results suggest that the increase in local and surrounding brain tissue absorption was due to the focal bicuculline methiodide induced seizure rather than other factors such as stab cortex tissue wound injection. Epileptiform events, including interictal spikes, ictal onset and spread were identified in near real time. To the best of our knowledge, this is the first experimental evidence for millisecond temporal resolution, micron scale imaging, and centimeters depth, of focal seizure onset and spread by a noninvasive technique.

Quantitative photoacoustic image reconstruction can be used to resolve the light scattering problem with the deeper penetration in the tissue based on compensating the reconstructed image with a pre-calculated optical fluence distribution(Yuan et al. 2007, Yao et al. 2009). It is possible to achieve higher resolution at cellular and even sub-cellular levels to image the neuronal circuitry *in vivo* by use of photoacoustic microscopy at a depth of more than three millimeters(Shelton and Applegate , Hu et al. 2010). The findings imply that PAT has potential for noninvasive real time brain mapping of cortical processing and seizures.

A key advantage of our noninvasive PAT system for epileptiform event monitoring is the real time imaging ability. Seizures are generated by complex interactions of a large group of neurons in which the population of neurons involved varies largely from moment to moment(Schwartz and Bonhoeffer 2001). By achieving 1,000 times faster data acquisition of the current PAT imaging system relative to our previous PAT system (Zhang et al. 2008), we were able to observe that the spatial aspects of the seizure focus varied over time as suggested by the changes in hemodynamics (Fig. 3c). At present, the imaging speed was

limited only by the 10 Hz laser pulse-repetition-rate. Since considerably faster lasers of ~500 Hz pulse-repetition-rates are now commercially available, the temporal resolution of PAT will soon reach a level of a few milliseconds. This, coupled with the compactness of an optical system will make it possible to bring a PAT system to the bedside for real-time and chronic monitoring of seizures in infants or during extra-operative epilepsy brain mapping, for example.

One hypothesis is that long-standing epilepsy may lead to the development of secondary epileptogenic regions located at a site distant from the original focus, a factor that may reduce the likelihood of successful epilepsy presurgical planning (Cendes et al. 1995). The ability to identify the epileptic focus and associated network may lead to better epilepsy surgery outcomes for many individuals. Various methods such as cross correlation and Granger causality have been explored for assessing the dynamic directional relationships among brain regions using time series data(Kaminski et al. 2001, Bressler et al. 2008). We used Granger causality as a way to quantify the dynamic interactions amongst the primary seizure focus, secondary seizure foci, and middle cerebral artery based on the time-series photoacoustic data. Specifically, Granger causality allowed for assessment of the magnitude and direction of temporal relationships during overlapping PAT time-series windows. Results further exemplified the temporal aspects of seizure onset, seizure secondary spread, and seizure termination. Collectively, PAT image analysis and tools for effective connectivity may result in a better understanding of epileptic networks at high spatiotemporal resolution.

Little data are available regarding a link between vascular changes and seizures (Ndode-Ekane et al.). We found that the vasomotor phenomena of micro blood vessels correlate with interictal spike and wave discharges (Fig. 5d). Interictal spikes generated a strong cerebral metabolic change that induced cerebral vessel dilation and a focal increase in cerebral blood flow provided oxygenated hemoglobin to hypermetabolic neurons, with a

13

corresponding increase in total hemoglobin(Ma et al. 2009). Vasomotion during seizure onset and spread was clearly caused by the oscillation in vessel diameter and the expansion of the vessel cross section. We reasoned that the dilation resulted in an active cerebral microvasculature response to increased metabolic activity accompanying the seizure(Myers and Intaglietta 1976). The combination of multi-scale imaging ability and endogenous hemoglobin contrast makes PAT a promising tool for imaging microvasculature during seizure onset. Future quantitative PAT studies will allow us to resolve many of the hemodynamic components, including changes in level of hemoglobin oxygenation (i.e., deoxy- and oxy-hemoglobin), cerebral blood flow, and the rate of cerebral oxygen metabolism, for a detailed understanding of the neurovascular coupling phenomenon, both during and in between seizures(Yuan et al. 2007, Yao et al. 2009).

The present work represents a major technological and scientific breakthrough in epilepsy. Previous attempts to track from moment to moment populations of neurons participating in an epileptiform event had not been possible with any technique or tool because of spatial and/or temporal sampling limitations. The high spatial and temporal sampling of the novel PAT system allowed for the first time the complete mapping of an epileptiform event *in vivo*. Another major breakthrough is that this is the first report of mapping an epileptiform event at depths well below the cortex. In terms of impact, this is the first demonstration of emerging optical mapping tool in the surgical evaluation of focal cortical epilepsy, since accurate localization of the epileptic focus, propagation paths, and subcortical networks critically depends on the precise localization of epileptogenic neurons and networks. Clearly the use of our PAT system, experimental paradigm, results, and analyses advances our understanding of epilepsy and seizure temporal spatial properties relative to previous attempts. The noninvasive yet whole surface and depth capabilities of the PAT system allowed for the first time to actually see what is happening during

ictogenesis in terms of seizure onset and spread. The challenge of mapping focal epilepsy stems from the observation that the pathology associated with focal epilepsy is often distributed across a number of brain sites. Seizures in animal models and in people often have a multifocal or broadly synchronized onset. The implication of these observations is that each of the sites could act independently to initiate a seizure or, potentially, to drive another site into a seizure. The current study lends support to the theory that seizure onset and spread involves a rich interplay between multiple cortical and subcortical foci during the onset and spread of focal epilepsy. The findings are timely in the sense that the neuroscience community is questioning the long-held dogma that seizure onset involves some sort of single focus or epicenter in favor of the emerging thought that seizures instead involve multiple cortical and subcortical foci.

Acknowledgements

References

Berg, A. T., J. T. Langfitt, S. S. Spencer, and B. G. Vickrey. 2007. Stopping antiepileptic drugs after epilepsy surgery: a survey of U.S. epilepsy center neurologists. Epilepsy Behav **10**:219-222.

Bertram, E. H. 2009. Temporal lobe epilepsy: Where do the seizures really begin? Epilepsy & Behavior **14**:32-37.

Bertram, E. H., D. X. Zhang, P. Mangan, N. Fountain, and D. Rempe. 1998. Functional anatomy of limbic epilepsy: a proposal for central synchronization of a diffusely hyperexcitable network. Epilepsy Research **32**:194-205.

Birbeck, G. L., R. D. Hays, X. Cui, and B. G. Vickrey. 2002. Seizure reduction and quality of life improvements in people with epilepsy. Epilepsia **43**:535-538.

Bluestone, A. Y., G. Abdoulaev, C. H. Schmitz, R. L. Barbour, and A. H. Hielscher. 2001. Three-dimensional optical tomography of hemodynamics in the human head. Optics Express **9**:272-286.

Boas, D. A., T. Gaudette, G. Strangman, X. Cheng, J. J. Marota, and J. B. Mandeville. 2001. The accuracy of near infrared spectroscopy and imaging during focal changes in cerebral hemodynamics. Neuroimage **13**:76-90.

Bressler, S. L., W. Tang, C. M. Sylvester, G. L. Shulman, and M. Corbetta. 2008. Top-down control of human visual cortex by frontal and parietal cortex in anticipatory visual spatial attention. J Neurosci **28**:10056-10061.

Brovelli, A., M. Ding, A. Ledberg, Y. Chen, R. Nakamura, and S. L. Bressler. 2004. Beta oscillations in a large-scale sensorimotor cortical network: directional influences revealed by Granger causality. Proc Natl Acad Sci U S A **101**:9849-9854.

Cadotte, A. J., T. B. DeMarse, T. H. Mareci, M. B. Parekh, S. S. Talathi, D. U. Hwang, W. L. Ditto, M. Z. Ding, and P. R. Carney. 2010. Granger causality relationships between local field potentials in an animal model of temporal lobe epilepsy. Journal of Neuroscience Methods **189**:121-129.

Cendes, F., M. J. Cook, C. Watson, F. Andermann, D. R. Fish, S. D. Shorvon, P. Bergin, S. Free, F. Dubeau, and D. L. Arnold. 1995. Frequency and Characteristics of Dual Pathology in Patients with Lesional Epilepsy. Neurology **45**:2058-2064.

Denk, W., J. H. Strickler, and W. W. Webb. 1990. Two-photon laser scanning fluorescence microscopy. Science **248**:73-76.

Duncan, J. S., J. W. Sander, S. M. Sisodiya, and M. C. Walker. 2006. Adult epilepsy. Lancet **367**:1087-1100.

Engel, J. 2004. The goal of epilepsy therapy: No seizures, no side effects, as soon as possible. Cns Spectrums **9**:95-97.

Fisher, R. S., W. V. Boas, W. Blume, C. Elger, P. Genton, P. Lee, and J. Engel. 2005. Epileptic seizures and epilepsy: Definitions proposed by the International League against Epilepsy (ILAE) and the International Bureau for Epilepsy (IBE). Epilepsia **46**:470-472.

Fountain, N. B., J. Bear, E. H. Bertram, and E. W. Lothman. 1998. Responses of deep entorhinal cortex are epileptiform in an electrogenic rat model of chronic temporal lobe epilepsy. Journal of Neurophysiology **80**:230-240.

Granger, C. W. J. 1969. Investigating Causal Relations by Econometric Models and Cross-Spectral Methods. Econometrica **37**:414-&.

Greenfield, J., Geyer, J., Carney, P.R. 2011. *Reading EEGs: A Practical Approach*. Lippincott Wilkins Raven, Philadelphia.

Grinvald, A., R. D. Frostig, E. Lieke, and R. Hildesheim. 1988. Optical Imaging of Neuronal-Activity. Physiological Reviews **68**:1285-1366.

Haglund, M. M. and D. W. Hochman. 2004. Optical imaging of epileptiform activity in human neocortex. Epilepsia **45**:43-47.

Haglund, M. M., G. A. Ojemann, and D. W. Hochman. 1992. Optical imaging of epileptiform and functional activity in human cerebral cortex. Nature **358**:668-671.

Hauser, W. A. 1992. Seizure disorders: the changes with age. Epilepsia **33 Suppl 4**:S6-14.

Hauser, W. A. and L. T. Kurland. 1975. The epidemiology of epilepsy in Rochester, Minnesota, 1935 through 1967. Epilepsia **16**:1-66.

Hill, D. K. and R. D. Keynes. 1949. Opacity Changes in Stimulated Nerve. Journal of Physiology-London **108**:278-281.

Hu, S., B. Rao, K. Maslov, and L. V. Wang. 2010. Label-free photoacoustic ophthalmic angiography. Optics Letters **35**:1-3.

Huang, D., E. A. Swanson, C. P. Lin, J. S. Schuman, W. G. Stinson, W. Chang, M. R. Hee, T. Flotte, K. Gregory, C. A. Puliafito, and J. G. Fujimoto. 1991. Optical Coherence Tomography. Science **254**:1178-1181.

Jeha, L. E., I. Najm, W. Bingaman, D. Dinner, P. Widdess-Walsh, and H. Luders. 2007. Surgical outcome and prognostic factors of frontal lobe epilepsy surgery. Brain **130**:574-584.

Jiang, H. B., K. D. Paulsen, U. L. Osterberg, B. W. Pogue, and M. S. Patterson. 1996. Optical image reconstruction using frequency-domain data: Simulations and experiments. Journal of the Optical Society of America a-Optics Image Science and Vision **13**:253-266.

Kaminski, M., M. Z. Ding, W. A. Truccolo, and S. L. Bressler. 2001. Evaluating causal relations in neural systems: Granger causality, directed transfer function and statistical assessment of significance. Biological Cybernetics **85**:145-157.

Khalilov, I., G. L. Holmes, and Y. Ben-Ari. 2003. In vitro formation of a secondary epileptogenic mirror focus by interhippocampal propagation of seizures. Nat Neurosci **6**:1079-1085.

Kruger, R. A. and P. Y. Liu. 1994. Photoacoustic Ultrasound - Pulse Production and Detection in 0.5-Percent Liposyn. Medical Physics **21**:1179-1184.

Laufer, J., D. Delpy, C. Elwell, and P. Beard. 2007. Quantitative spatially resolved measurement of tissue chromophore concentrations using photoacoustic spectroscopy: application to the measurement of blood oxygenation and haemoglobin concentration. Phys Med Biol **52**:141-168.

Ma, H., M. Zhao, M. Suh, and T. H. Schwartz. 2009. Hemodynamic surrogates for excitatory membrane potential change during interictal epileptiform events in rat neocortex. J Neurophysiol **101**:2550-2562.

Mangan, P. S., C. A. Scott, J. M. Williamson, and E. H. Bertram. 2000. Aberrant neuronal physiology in the basal nucleus of the amygdala in a model of chronic limbic epilepsy. Neuroscience **101**:377-391.

Myers, R. R. and M. Intaglietta. 1976. Brain Microvascular Hemodynamic Responses to Induced Seizures. Stroke **7**:83-88.

Ndode-Ekane, X. E., N. Hayward, O. Grohn, and A. Pitkanen. Vascular changes in epilepsy: functional consequences and association with network plasticity in pilocarpine-induced experimental epilepsy. Neuroscience **166**:312-332.

Oleary, M. A., D. A. Boas, B. Chance, and A. G. Yodh. 1995. Experimental Images of Heterogeneous Turbid Media by Frequency-Domain Diffusing-Photon Tomography. Optics Letters **20**:426-428.

Paxinos, G. W., C. 1998. The rat brain. Academic Press.

Schwartz, T. H. and T. Bonhoeffer. 2001. In vivo optical mapping of epileptic foci and surround inhibition in ferret cerebral cortex. Nat Med **7**:1063-1067.

Shelton, R. L. and B. E. Applegate. Ultrahigh resolution photoacoustic microscopy via transient absorption. Biomed Opt Express **1**:676-686.

Sipkins, D. A., X. B. Wei, J. W. Wu, J. M. Runnels, D. Cote, T. K. Means, A. D. Luster, D. T. Scadden, and C. P. Lin. 2005. In vivo imaging of specialized bone marrow endothelial microdomains for tumour engraftment. Nature **435**:969-973.

Sokol, D. K., O. N. Markand, E. C. Daly, T. G. Luerssen, and M. D. Malkoff. 2000. Near infrared spectroscopy (NIRS) distinguishes seizure types. Seizure **9**:323-327.

Steinhoff, B. J., G. Herrendorf, and C. Kurth. 1996. Ictal near infrared spectroscopy in temporal lobe epilepsy: a pilot study. Seizure **5**:97-101.

Thom, M., G. W. Mathem, J. H. Cross, and E. H. Bertram. 2010. Mesial Temporal Lobe Epilepsy: How Do We Improve Surgical Outcome? Annals of Neurology **68**:424-434.

Wang, X., Y. H. Chen, S. L. Bressler, and M. Z. Ding. 2007. Granger causality between multiple interdependent neurobiological time series: Blockwise versus pairwise methods. International Journal of Neural Systems **17**:71-78.

Watanabe, E., A. Maki, F. Kawaguchi, Y. Yamashita, H. Koizumi, and Y. Mayanagi. 2000. Noninvasive cerebral blood volume measurement during seizures using multichannel near infrared spectroscopic topography. J Biomed Opt **5**:287-290.

Xiang, L. Z., D. Xing, H. M. Gu, D. W. Yang, S. H. Yang, L. M. Zeng, and W. R. Chen. 2007. Real-time optoacoustic monitoring of vascular damage during photodynamic therapy treatment of tumor. Journal of Biomedical Optics **12**.

Yao, L., Y. Sun, and H. B. Jiang. 2009. Quantitative photoacoustic tomography based on the radiative transfer equation. Optics Letters **34**:1765-1767.

Yuan, Z., Q. Wang, and H. B. Jiang. 2007. Reconstruction of optical absorption coefficient maps of heterogeneous media by photoacoustic tomography coupled with diffusion equation based regularized Newton Method. Optics Express **15**:18076-18081.

Zhang, Q. Z., Z. Liu, P. R. Carney, Z. Yuan, H. X. Chen, S. N. Roper, and H. B. Jiang. 2008. Non-invasive imaging of epileptic seizures in vivo using photoacoustic tomography. Physics in Medicine and Biology **53**:1921-1931.

Zhou, J., S. S. Talathi, A. Cadotte, Z. Liu, G. L. Holmes, and P. R. Carney. 2009. The Effects of Hippocampus Ca1 Single Neuron Firing Properties on Interictal Spike Patterns during Seizure Onset in a Rat Model of Temporal Lobe Epilepsy. Epilepsia **50**:317-317.

Figure Legends

Figure 1 | Real-time PAT system for seizure dynamics. (a.) Schematic of the real time PAT system. A 192-element full-ring transducer array was used to capture the PA signal during seizure onset. Using 64-channel parallel data acquisition and 3:1 electronic multiplexing, imaging speed was up to 0.33sec/frame (Supplemental Figure 1). The spatial resolution of this imaging system was ~150 microns (Supplemental Figure 2). (b.) Noninvasive PAT imaging of a rat brain *in vivo* with the skin and skull intact. MCA, middle cerebral artery; RH, right hemispheres; LH, left hemispheres; LOB, left olfactory bulbs; ROB, Right olfactory bulbs. (c.) Open-skull photograph of the rat brain surface acquired after the PAT experiment. Numbers 1–5 indicate the corresponding blood vessels in the PAT image and rat brain photograph.

Figure 2 | Noninvasive epileptic foci localization. (a.) EEG recordings of seizure onset after BMI injection. (b.) Schematic showing the location of BMI injection and saline injection (control). B, BMI injection; S, saline injection. (c.) Reconstructed PAT image before (left) and after (right) the BMI injection. The BMI and saline were injected into the left and right parietal neocortex, respectively. A significant increase of optical absorption is seen in the region of the BMI injection, while no absorption contrast is observed in the region of the saline injection relative to its surroundings. (d.) Series of PAT images from three representative transverse planes parallel to the skin surface with 755 nm wavelength. Slices 5, 7, and 9 are the images obtained 3, 5 and 7 mm under the skin, respectively. The images show different spatial patterns at the seizure foci at different tomographic layers. (e.) Three-dimensional rendering of the epileptic foci from different tomographic layers (Web Supplement, Movie S1).

Figure 3 | Real-time monitoring of ictal onset. (a.) A PAT image showing the cerebral vasculature and the position of BMI injection. ROI, region of interest; Scale bar: 2mm. (b.) EEG recordings showing the seizure onset about 1 min after BMI injection. (c.) PAT images recording the ictal onset in real time. At 1min 6.267 s the area of the focus was 0.2053 mm^2. The area of the focus then increased in size over the next 2 s to 0.5004mm^2, corresponding to an increase in the amplitude of the EEG spikes. The area of the seizure focus was derived from the PAT images by thresholding to a pixel value one standard deviation above the pixel values from the area of the focus during the control conditions. Scale bar: 500μm (Web Supplement, Movie S2).

Figure 4 | *In vivo* **Maps of mirror foci propagation**. (a.) Left, the PA image of the rat brain; the yellow dotted rectangular shows the ROI for analysis; Right, noninvasive imaging of the primary and secondary seizure foci in bilateral homotopic cortex. a_{1-4} shows how mirror foci were generated and diminished. The PA signal in the secondary seizure foci was smaller in magnitude and delayed in time compared to the signal recorded from the primary foci. (b.) Left, Granger analysis of the image around the foci and its 'surround' area; Right, PA signal from the foci (red) and surround (blue) during an ictal event. The PA signal surrounding the foci (blue line) shows inverted signal compared to that from the seizure foci (red line) corresponding to neuronal inhibition. (c.) Granger analysis of the seizure foci, secondary seizure foci and middle cerebral artery. c_1, a PAT image showing the nine selected ROIs; c_2, connectivity relation between the primary and secondary seizure foci; c_3, connectivity relation between the primary focus, secondary seizure foci and middle cerebral artery. The line width stands for the relative Granger causal influence strength.

Figure 5 | Changes of blood vessel diameter during interictal onset. (a.) PA image of the rat cortex vasculature with the intact scalp and skull. The red arrow indicates the microvascularity (MV) along the yellow dashed line direction for a cross-sectional scanning

using a 50 MHz ultrasound transducer. (b.) Typical photoacoustic signals from the targeted vessel at different times. (c.) EEG recordings show the interictal spikes and (d.) Change of the vessel size captured by PAT. There was a clear correlation between the interictal spikes and the changes of the vessel size.

Supplement Figures

Figure 1 | Temporal resolution demonstration of the PAT system. Photoacoustic images depicting frames from a 10-second sequence of dynamic ink flow through a 0.3 mm diameter tube (Web Supplement, Movie S3). The movie shows that the temporal resolution of this imaging system was ~0.33 seconds/ frame.

Figure 2 | Spatial resolution measurement of the PAT system. (a.) Cross-sectional PA image of a two-copper-rods phantom. The two copper rods (diameter: 0.05mm) were embedded in a cylindrical tissue–mimicking phantom at a depth of 10 mm. The center-to-center distance between the two copper rods was approximately 2.2 mm. (b.) The normalized profile of the reconstructed PA image shown in (a.) along y=10 mm. The half- and quarter-amplitude widths were obtained by measuring the distance between points AB and between CD, respectively. The spatial resolution of the imaging system calculated with Rayleigh's law was 150μm.
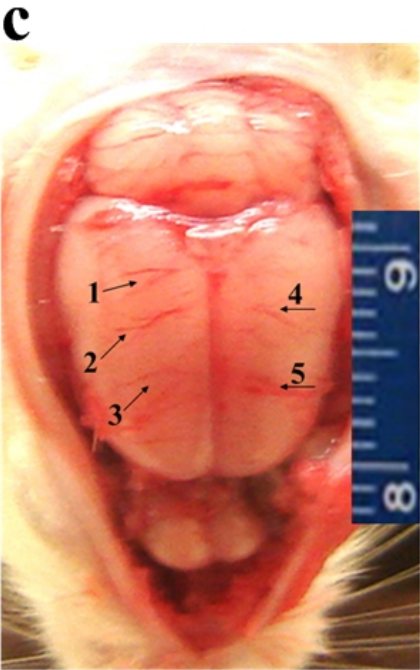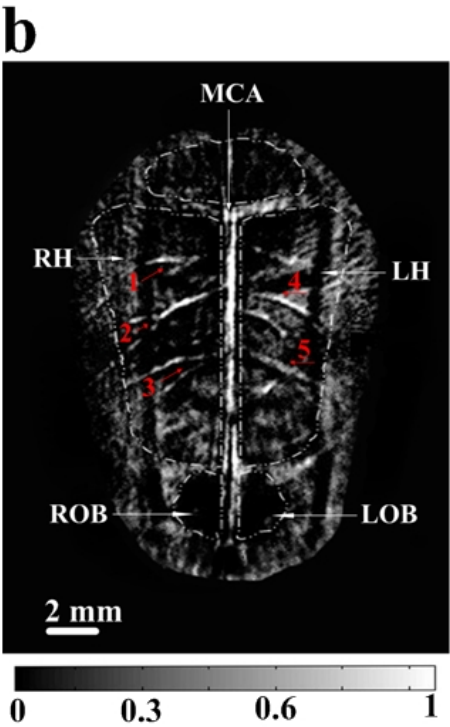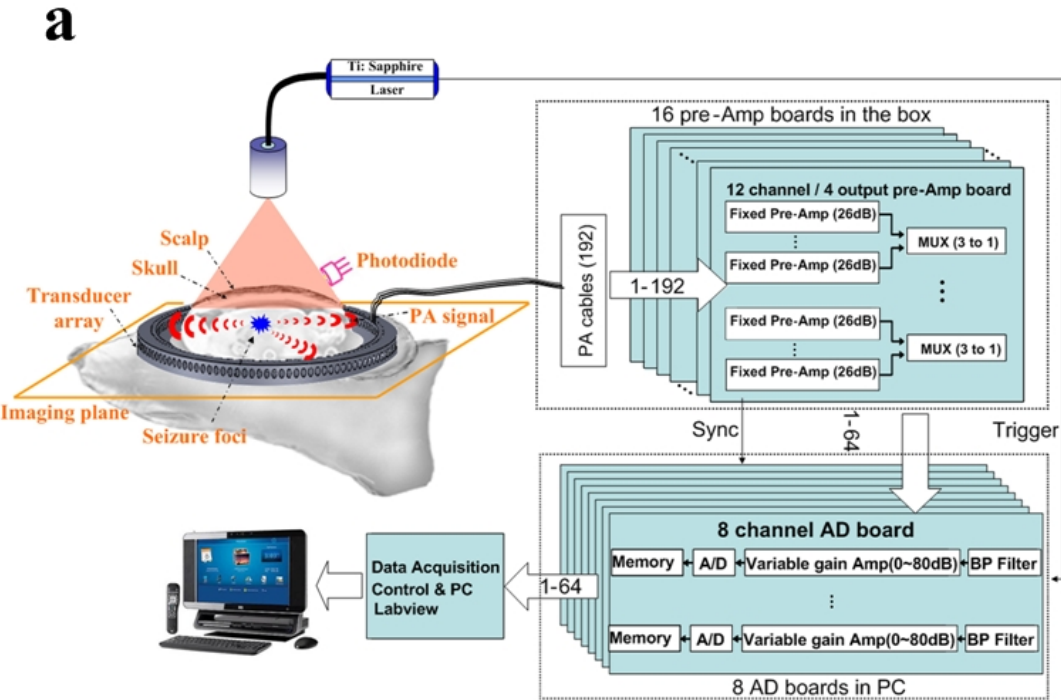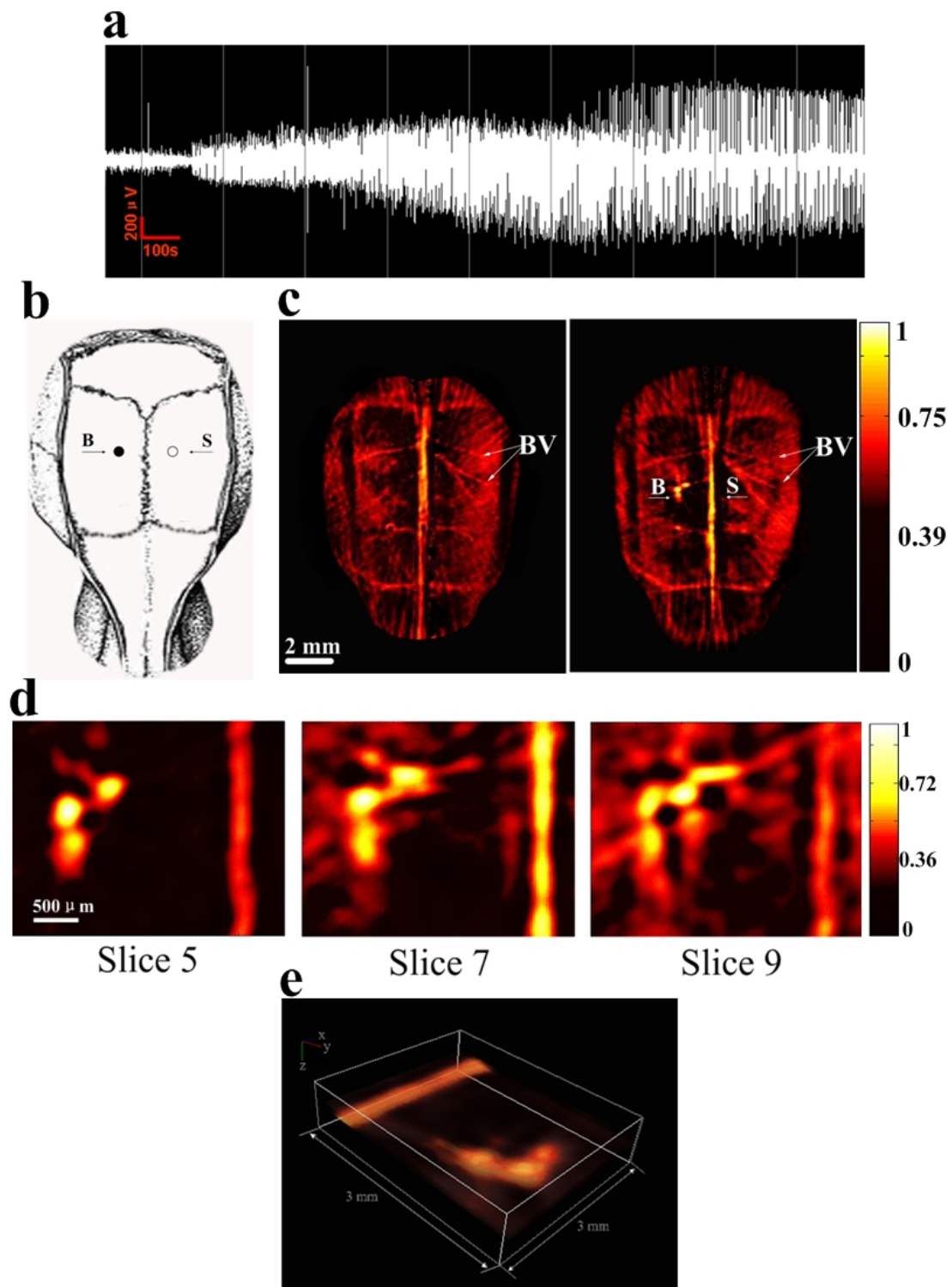
Figure 1

Figure 2

Figure 3

a

2 mm

b

200 μV
20s

c

| 65.934 Sec
0 mm² | 1min 6.267 Sec
0.2053 mm² | 1min 6.600 Sec
0.2342 mm² | 1min 6.933 Sec
0.2670 mm² |

1min 7.266 Sec
0.3877 mm²

1min 7.599 Sec
0.3986 mm²

1min 7.932 Sec
0.4234 mm²

1min 8.265 Sec
0.5004 mm²

500 μm
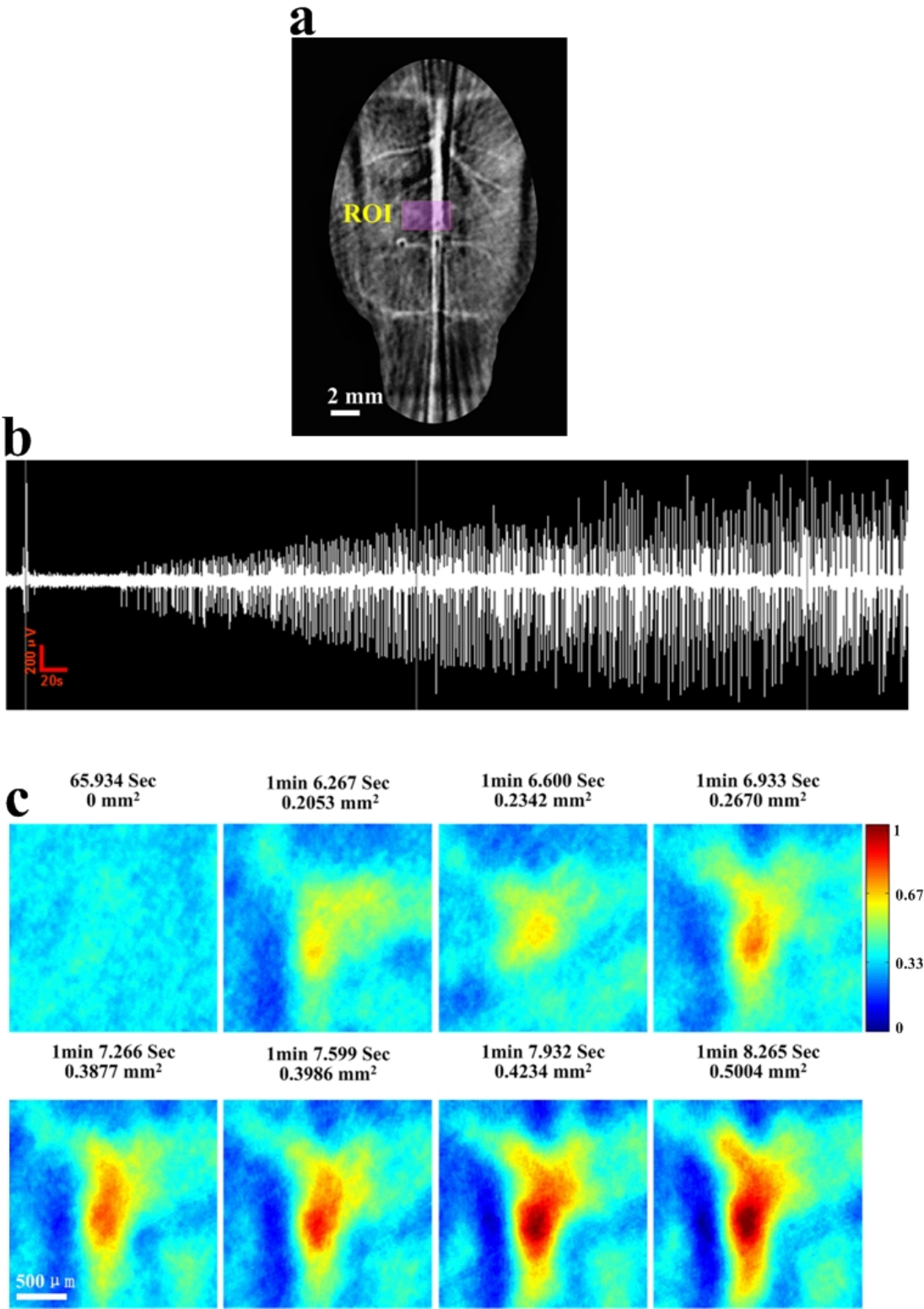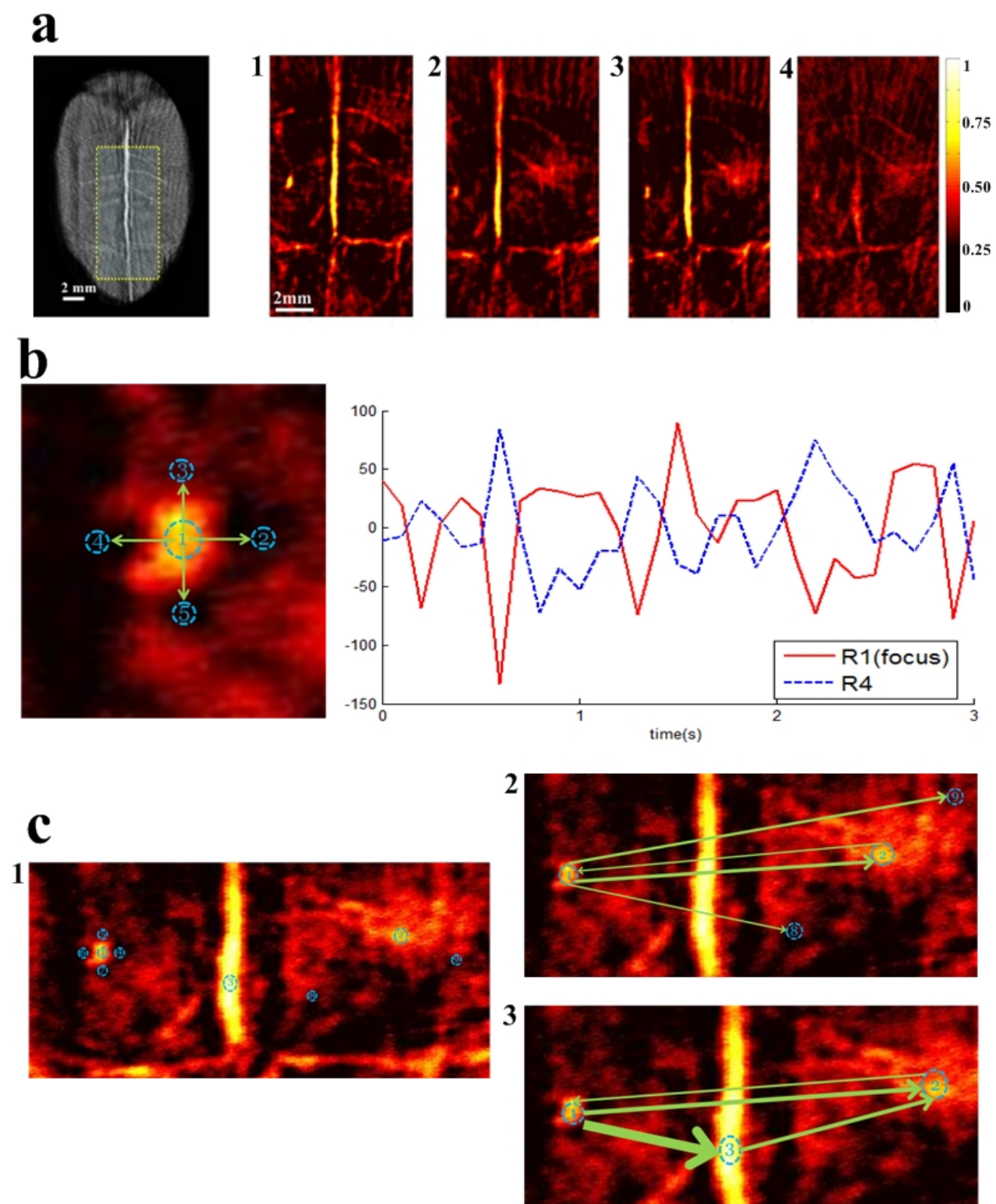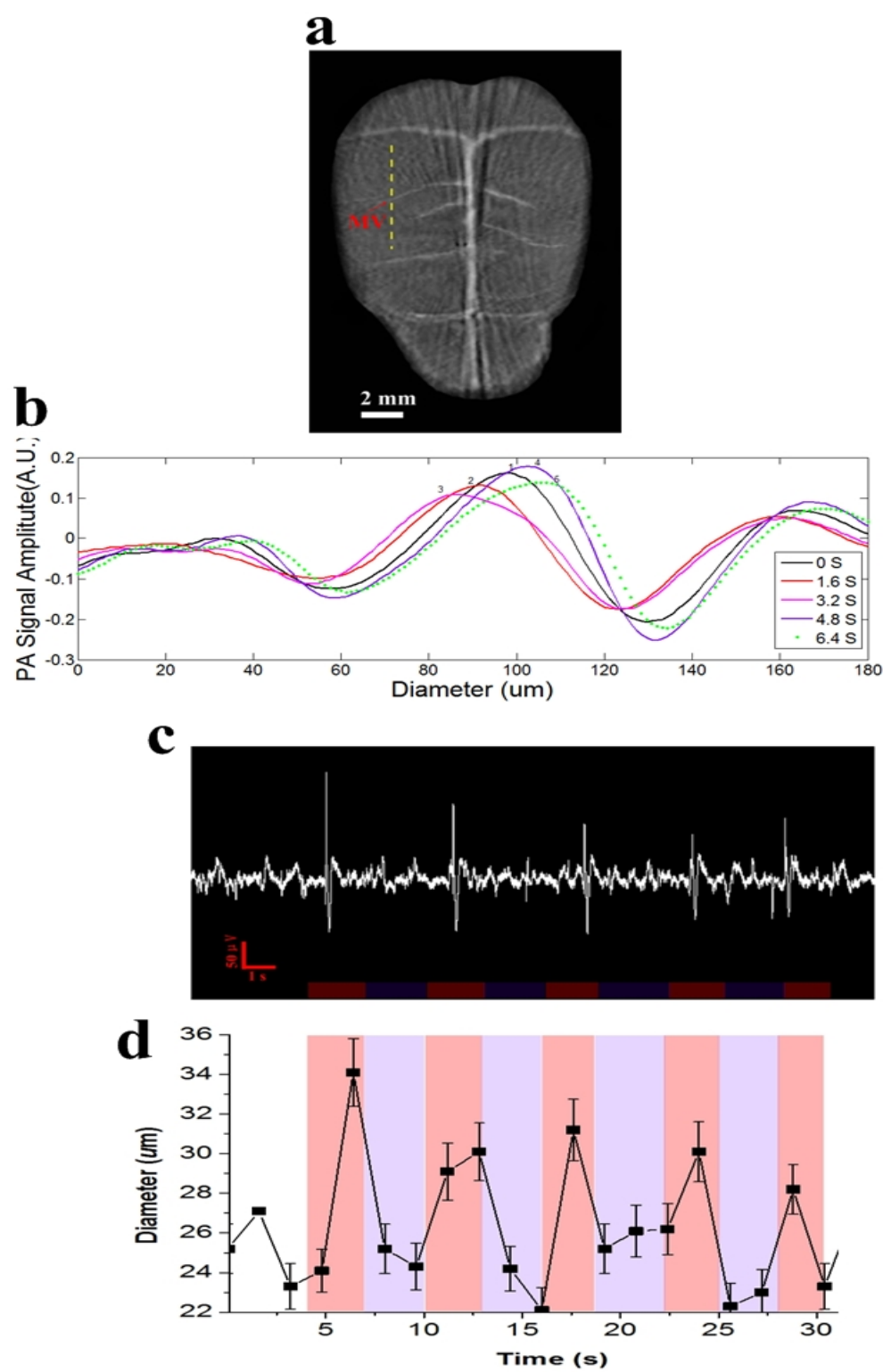
Figure 4

Figure 5

Supplemental Figures

Figure 1

Figure 2